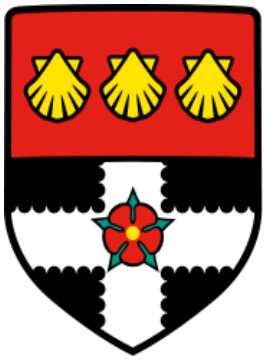

UNIVERSITY OF READING

School of Mathematical, Physical and Computational Sciences

Department of Meteorology

The value of observations for forecasting convective rainfall

Xinyue Yao

Supervisor

Prof. Bob Plant

Dr Alison Fowler

17th August 2020

A dissertation submitted in partial fulfilment of the requirement for the degree of MSc Applied Meteorology

Acknowledgements

I would like to say thanks, thanks and many thanks to my supervisor Prof. Bob Plant and Dr Alison Fowler for their time, patient guidance and insightful comments. This piece of work which I am very proud of could not be accomplished without their patient explanation from the basic statistical issues to the interpretation of the results. Also, many thanks to my companion and family for their cares and kind encouragements during these lonely and stressful days.

Abstract

Assimilation of observations acts as an essential part in convective-scale numerical weather prediction (NWP). However, an increasingly dense observing network is providing a vast quantity of daily observing data, imposing computational challenges to the data assimilation (DA) system. Understanding the contribution of each observation in DA benefits the deployment and selection of observations in the real world. This thesis uses the observational influence matrix as a diagnostic tool to monitor the sensitivity of analysis to the observations in the presence of convection and precipitation. A set of 'twin experiments' are conducted in an idealised fluid model developed by Kent *et al.,* (2017). The model modifies the shallow water equations (SWEs) and is able to represent the dynamics of two basic scenarios: Rossby adjustment and non-rotating flow over topography. The self-sensitivities of each variable and the cross-sensitivities between variables are calculated and analysed at each assimilation cycle for both scenarios.

Results show the overall influence of the observing system accounts for around 20% of the analysis, which is comparable to the typical observational influence in operational DA. Observations of pressure and rain mass are more valuable near convective cores while less influential in geostrophically-balanced regions. Similarly, the self-sensitivities of winds are large at places with dramatic variations of windspeed. It is shown that the observational density also impacts the behaviour of observations in DA. That is the observational influence is high in data-sparse regions while low in data-rich areas, which is attributed to the idea of 'data redundancy'. Overall, observations of pressure are found to be the most influential type in this study, however their influence can be compensated by other observational types when removed from the observational system. Lastly, this study demonstrates the importance of a well-tuned system for the interpretation of the observational influence diagnostic. In the Rossby adjustment scenario, the ensemble spread is found to be insufficient, as such the observations are given progressively less weight in the data assimilation than they would have received with a well-tuned ensemble. These results provide insight into how observations can be utilised in the most beneficial way for operational convective-scale DA.

Key words: Observational influence, self-sensitivity, data assimilation, fluid model, Rossby adjustment, non-rotating flow over topography

List of Abbreviations

NWP	Numerical Weather Prediction
DA	Data assimilation
SWEs	Shallow Water Equations
CPMs	Convection Permitting Models
modRSW	Modified Rotating Shallow Water
LFC	Level of Free Convection
EnKF	Ensemble Kalman Filter
RMSE	Root Mean Square Error
SPR	Spread
LS	Least Squares
OID	Observation Influence Diagnostic
PAI	Partial Influence

Contents

Chapter 1

Introduction

This chapter provides an overview of the motivations behind the study of this thesis, illustrating the observational issues in data assimilation and the necessity for investigating the observational influence in the presence of convection.

1.1 Motivation

Accurately estimating the state of the atmosphere is never an easy problem. Usually one is provided with imperfect background information, model forecast, and separate real-time observations. Data assimilation (DA) offers a means to optimise the initial condition by combining the model forecast with meteorological observations, taking into account their respective uncertainties (Kent *et al.*, 2017). Since satellites, radar and other innovations in observations are becoming much cheaper than before, today's observing network is becoming ever denser, providing a vast quantity of daily observations, which imposes computational and scientific challenges to DA system and therefore forecast abilities. Hence, better knowledge is required on the important role of observations in DA, what kind of observations are most significant for weather prediction and where to put priorities and resources (Necker *et al.,* 2019).

Relevant studies have been conducted to investigate the value of observations in forecasts, based on a global view. For example, Cardinali *et al.,* (2004) estimated that for a typical global forecast model, around 18% of the DA analysis is attributable to the assimilated observation, which means that for synoptic scales, observations act as an adjustment of the prior model forecast to make it closer to the truth, rather than a replacement. (The basis for making such an estimate is discussed in Section 3.3.2). However, few researches have focused on the observational influence in a limited region with convective activities. This raises questions about the observation influence on the forecast on a convective scale, which is much more difficult to resolve than large scales. Will the observations be more valuable to DA or not? It is worth investigating such a topic since measurement of observational influence benefits the understanding

of DA and hence the model forecast ability which is crucial particularly in coping with hazardous convective weather.

1.2 Project aims

In this study, a fluid dynamic model with its DA system proposed by Kent *et al.*, (2017) is applied to assess the performance of DA, as well as the value of different observational variables (pressure, winds and rain mass) in the presence of convection and precipitation. Via the results of these experiments, the thesis aims to answer the following questions:

1. How important are the observations of each variable in DA in convective regions? What are the requirements for the observational density for the different variables?
2. How much would the influence of the observing system change if one influential observational type is removed?
3. How does the observation influence correspond to the accuracy of the analysis? Does each observation give optimal influence on the forecast?

1.3 Outline

The outline of this thesis is as follows. In section 2, a brief review of the evolution of forecasts of convective rainfall is given. Section 3 discusses in depth the construction and the dynamics of the idealised fluid model and the theory of ensemble Kalman filtering, along with the diagnostics for assessing the observational influence in DA system. The experimental design for different model scenarios and the set-up of the model parameters are presented in Section 4. The results addressing the above questions are discussed in detail in Section 5. Finally, section 6 provides a conclusion of the results, along with potential directions for further researches in the future.

Chapter 2

How is convective rainfall forecasted?

Damage from extreme convective rainfall disrupts normal life and imposes financial burdens of individuals and local society, indicating the importance of accurate forecast of convective-scale precipitation (Schroeer and Tye, 2019). However, the long evolution of weather forecasting proves that predicting weather has never been an easy task, especially at a convective scale. Numerical weather prediction (NWP) models have been utilised to produce rainfall forecast for more than 50 years (Clark *et al.,* 2016). NWP can be simply defined as the process of predicting the weather based on the observations of current atmospheric conditions, as well as the 'first guess' of forecast models, which is generated from a previous short-term forecast using a numerical integration of physical laws representing atmospheric dynamics and thermodynamics (Clark *et al.,* 2016).

Traditional NWP models which focus on synoptic scales of motion, such as midlatitude cyclones and fronts, suffer from restrictions when simulating convective-scale processes. One of the biggest restrictions is that with horizontal grid spacing normally larger than 10 km, the physical laws inside the model are based on hydrostatic and geostrophic balance (White *et al.,* 2005). However, these balances can no longer describe the convection since the vertical acceleration starts to affect the convective activities. Also, due to the low resolution, these large-scale models rely on convective parameterisation schemes to represent the impacts of deep convections on the synoptic-scale flow. Normally the parameterisation schemes treat updrafts and downdrafts as plumes that entrain and detrain, based on the idea of mass conservation (Pradhan *et al.*, 2018). However, since the cloud evolution is parameterised and flow is not identifiable in model grids, the parameterisation of deep convections is regarded as a major source of uncertainties in large-scale models (Prein *et al.,* 2015). For example, Prein *et al.,* (2013) and Brockhaus *et al.,* (2008) argued that the convection parameterisation leads to an underestimation of hourly precipitation intensities and the misrepresentation of the diurnal cycle of precipitation, and Berg *et al.,* (2013) suggested that the frequency of weak precipitation event is normally overestimated in large-scale models.

NWP models have been largely improved due to the steady increase in computing power over the last few decades, allowing the running of operational NWP models with horizontal grid space being restricted to less than 4 kilometres (Sun *et al.*, 2014). Models with higher resolutions provide the possibility of explicitly representing the convective activities without the need for convective parameterisation. This kind of models are referred to as convection-permitting models (CPMs) which operate on kilometer scale (Prein *et al.,* 2015). CPMs manage to 'see' the evolution of convection, but cannot well represent individual convective storms, since deep convection with a typical horizontal scale of 1-5 km usually takes up very few grid points in the model. Hence it is 'convection permitting' rather than 'convection resolving'.

Unlike models using the convective parameterisation schemes, CPMs allow the unstable growth of convective clouds on the grid. In a typical convective process, release of latent heat through condensation may allow a few grid points of the model to become buoyant with respect to its surroundings, leading to the evolution of vertical circulations and then the formation of deep clouds. In practice, such models often contain a parameterisation of partial cloud cover, enabling condensation to occur when the 'resolved' flow (updraughts, cloud-scale downdraughts and larger-scale subsidence) is not yet saturated (Clark *et al.,* 2016). In addition, CPMs allow a better representation of fine-scale orography and surface fields which is significant for the initiation of convection in mountainous areas or regions with heterogeneous land surfaces (Fosser, Khodayar and Berg, 2014; Prein *et al.,* 2015). Figure 2.1 shows the benefit of predicting convection precipitation using CPMs. Each grid in the global model calculates the rainfall independently through a parameterisation scheme, resulting in a general likelihood and areas of presence of precipitation rather than the explicit description of what the convective cells would look like. In contrast, the UKV CPM with 1.5 km grid space manages to produce a more explicit location of lines of shower as well as small-scale cells.

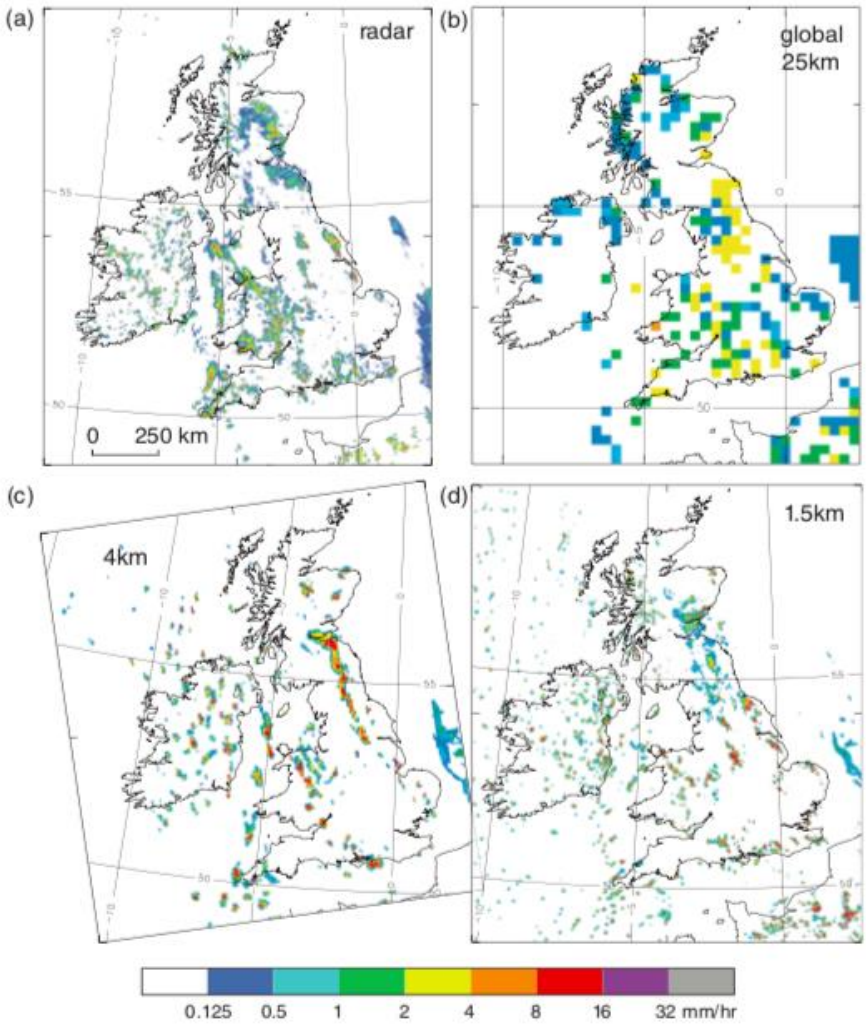

Figure 2.1: Case of convective precipitation over the UK on 8 July 2014 from (a) Radar, (b) Met UM Global model (T+12), (c) Euro 4 (T+12) and (d) UKV T+9 (1.5 km convection-permitting model). From Clark *et al.*, (2016).

However, it also shown in Figure 2.1 that even a high-resolution model cannot produce perfect forecasts by comparing with the radar image. Lorenz (1963) demonstrated the chaotic characteristic of the atmosphere, which will lead to the rapid growth of small errors in the initial conditions. Thus, atmospheric predictability has an upper limit even if the forecast model and its physical laws are perfect. This emphasizes the necessity of regular re-initialisation of the model using updates from observations. Also, to assess the uncertainties of the forecast, an ensemble of forecasts is usually constructed to provide a range of possible solutions for further states.

Chapter 3

Idealised fluid model and data assimilation

3.1 Idealised fluid model

3.1.1 Classical shallow water equations

The shallow water equations (SWEs) are widely used to understand the dynamics of Earth's atmosphere and oceans. They describe the motion of an incompressible thin layer of fluid of constant density in hydrostatic balance. A constant or variable Coriolis parameter may be used, and the layer is bounded by the bottom topography below and a free surface above (Zeitlin, 2007). The equations are derived from Navier-Stokes equations, assuming that the horizontal length scale is much larger than the vertical length scale, which means that the depth of flowing fluid, under the condition of mass conservation, is much less than the wavelength of disturbance brought to the free surface (Kent *et al.*, 2017).

Based on a Cartesian f-plane where dynamical variables are independent along one coordinate, the standard SWEs for variations only in the x coordinate can be described by the following equations (see Kent *et al.*, (2017)):

$$\partial_t h + \partial_x(hu) = 0, \tag{3.1a}$$

$$\partial_t(hu) + \partial_x(hu^2 + p(h)) - fhv = -gh\partial_x b \tag{3.1b}$$

$$\partial_t(hv) + \partial_x(huv) + fhu = 0, \tag{3.1c}$$

where $h = h(x,t)$ represents the space- and time-dependent fluid depth, $b = b(x)$ is the given height of bottom topography (so that the height of free surface is expressed as $h(x,t) + b(x)$), $u(x,t)$ and $v(x,t)$ are the horizontal wind velocity in the zonal and meridional directions, $p(h)$ is the effective pressure term, with the standard form as $p(h) = \frac{1}{2}gh^2$, and f and g are Coriolis parameter and gravitational acceleration respectively. Compared to a purely one-dimensional model, this series of equations add features of transverse flow v and Coriolis effects, allowing the simulation of more

sophisticated dynamics relevant to rotating fluids, such as geostrophic wind, while remaining computationally inexpensive.

3.1.2 Modified shallow water model

Kent *et al.*, (2017) proposed a modified rotating shallow water (modRSW) model, mimicking the conditional instability and the transport of moisture through a rain mass fraction term 'r'. Moreover, the binary 'on-off' nature of convective cloud and precipitation, which is hard to resolve in most NWP models, is simulated in the form of two specific threshold heights. When fluid heights exceed certain thresholds, it can be seen as the onset of convection or precipitation and the classical shallow water dynamics are transformed into a simplified cumulus convection. The equations contained in modRSW model can be written as:

$$\partial_t h + \partial_x(hu) = 0, \tag{3.2a}$$

$$\partial_t(hu) + \partial_x(hu^2 + P) + h{c_0}^2\partial_x r - fhv = -Q\partial_x b, \tag{3.2b}$$

$$\partial_t(hv) + \partial_x(huv) + fhu = 0, \tag{3.2c}$$

$$\partial_t(hr) + \partial_x(hur) + h\tilde{\beta}\partial_x u + \alpha hr = 0, \tag{3.2d}$$

where the mass (Eq 3.2a) and hv momentum (Eq 3.2c) equations remain unchanged compared to the classical SWEs of the previous subsection. The hu momentum equation (Eq 3.2b) includes a 'rainwater mass potential', ${c_0}^2 r$, and modified effective pressure terms *P* and *Q*, which are defined as:

$$P(h;b) = \begin{cases} p(H_c - b), & for\ h + b > H_c, \\ p(h), & otherwise, \end{cases} \tag{3.3a}$$

$$Q(h;b) = \begin{cases} p'(H_c - b), & for\ h + b > H_c, \\ p'(h), & otherwise. \end{cases} \tag{3.3b}$$

Moreover, an equation for the rain mass fraction r (Eq 3.2d) is added to close the system, including advection and source and sink terms. The 'rain switch' term $\tilde{\beta}$ is expressed as below:

$$\tilde{\beta} = \begin{cases} \beta, & for\ h + b > H_r\ and\ \partial_x u < 0, \\ 0, & otherwise. \end{cases} \tag{3.4}$$

The positive constants α and β determine respectively the rates of removal and production of model 'precipitation' (which is represented via the rain mass fraction r). H_c and H_r ($H_c < H_r$) are critical heights for the onset of convection and precipitation respectively (see Figure 3.1).

When $h + b < H_c$ and r equals to zero initially, the model is restricted to the classical shallow model (Eq 3.1), and there is no model 'rain'. The first modification to the classical shallow water model occurs whilst the free surface height $h + b$ exeeds H_c in Eq 3.3, enabling the representation of cumulus convection. Initiation of convection in nature occurs when air parcels reach their level of free convection (LFC), where the latent heat is released due to condensation, causing the air parcel to achieve positive buoyancy and accelerate further upwards. This rising mechanism is represented through modifying the pressure terms (Eq 3.3) here: the modified pressure above H_c (which can be regarded as LFC), namely $p(H_c - b) = \frac{1}{2} g(H_c - b)^2$, is lower than the standard pressure $p(h) = \frac{1}{2} gh^2$ at the same height, owing to which the model is more easily able to reach some large values of h. Also, this in a sense implies the fluid is forced to rise, although a rising motion cannot be explicitly represented by the model since the SWEs do not contain the vertical velocity.

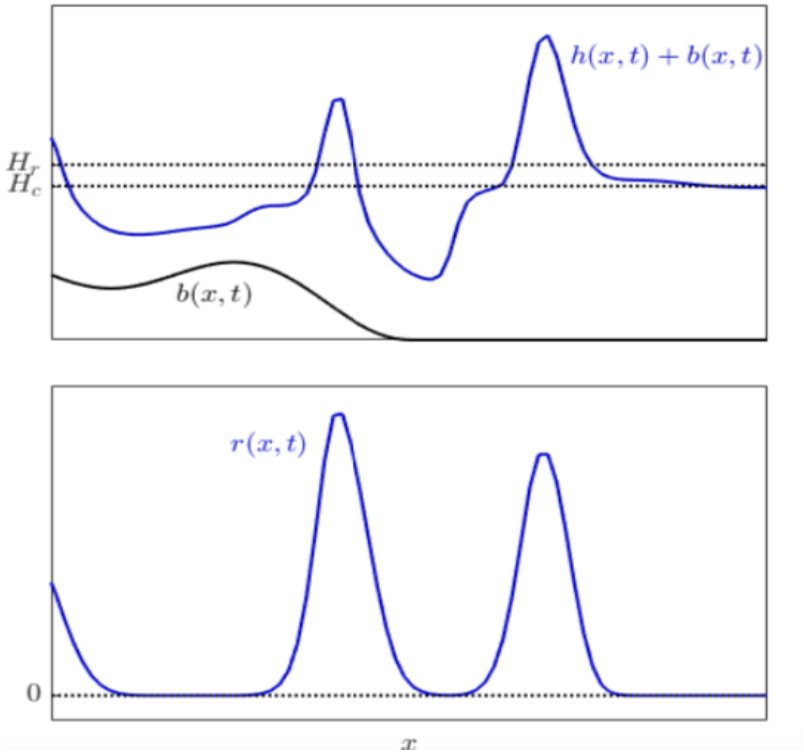

Figure 3.1. Schematic of free surface height (top) and model 'rain' r (bottom). The black dotted lines ($H_c < H_r$) are threshold heights for convection and precipitation. From Kent *et al.,* (2020).

Model 'precipitation' is produced ($r > 0$) when the height of free surface exceeds the second threshold H_r , which is slightly higher than H_c in order to ensure that precipitation occurs later than the onset of free convection. Meanwhile, there is also a requirement for horizontal wind convergence ($\partial_x u < 0$) for precipitation to form. The tunable parameter β (in Eq 3.4) controls the amount of precipitation produced. Once the model 'rain' forms, it feeds back to the hu momentum equation (Eq 3.2b) through term $h{c_0}^2 \partial_x r$ (${c_0}^2$ is tunable and controls the strength of the feedback), and is reduced through a linear sink term associated with the tunable parameter α (Eq 3.2d). It is demonstrated in Kent *et al.,* (2017) that the model 'rain' r can be thought of as the mass fraction of precipitated water that is active in the system, which is different from natural rain.

3.1.3 Model scenarios

The modRSW model applied in this project is designed to cover two major scenarios: (i) Rossby adjusted rotating flow and (ii) non-rotating flow over topography, both of which have rich histories of research in shallow water theory (Ford, 1994; Ward *et al.*, 2010).

Rossby adjustment dynamics illustrate the evolution of free surface height when a disturbance caused by a transverse jet is imposed on an initial rest state. The height field in the model evolves rapidly to adjust the initial momentum imbalance, including emitting gravity waves and shocks away from the jet core, before reaching geostrophic balance. Gravity waves are known to be generated also by deep convection and can give possible feedbacks on the initiation of convection, implying that the models based on SWEs are suitable to investigate the convective-scale phenomenon (Jewtoukoff, Plougonven and Hertzog, 2013; Kent *et al.,* 2017).

Figure 3.2 shows an example of gravity waves found in the experiments in Kent *et al.*, (2017): low-amplitude gravity waves can be seen propagating to the left of the convective cores in the left graph and in the Hovmoller plot of the evolution of h (the middle graph). Also, in real situations, multicellular convection systems can occur: these are most commonly found in midlatitudes and are characterised by repeated development of new cells along the gust front, which enables the survival of a large convective system (Markowski and Richardson, 2011; Kent *et al.,* 2017). This mechanism of this positive feedback can be basically represented in the model, as the gravity wave instigated here propagates to the left and can act to initiate a new region of weak convection and rainfall separated from the major convection. This is shown in the Hovmoller plot of the evolution of rainfall (the right graph in Figure 3.2) (see detail in Kent *et al.,* (2017)).

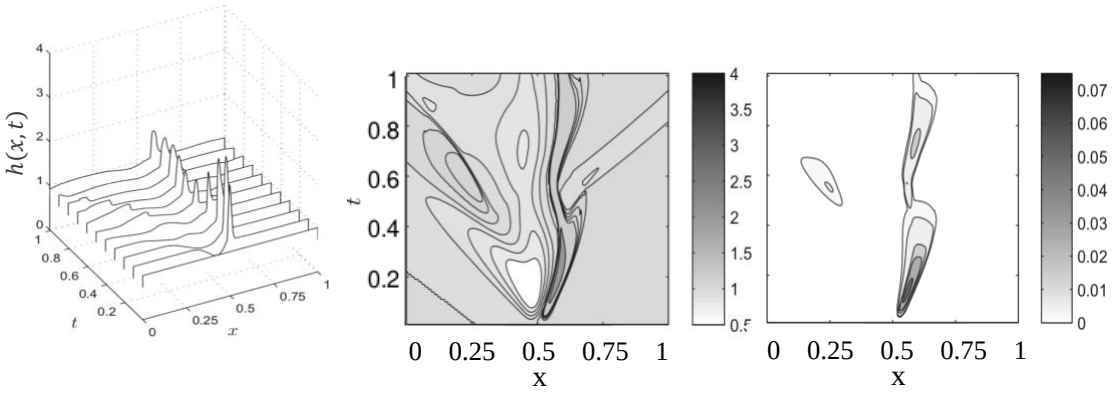

Figure 3.2: Time evolution of the height profile $h(x,t)$ (left) and the hovmoller plot of the evolution of the height profile $h(x,t)$ (middle) and the rainfall $r(x,t)$ (right). Adapted from Kent *et al.*, (2017).

Motivated by the experiments of Rossby adjustment scenario in Kent *et al.*, (2017) and Kent *et al.*, (2020), the shape of the initial profile of transverse *v*(*x*) used for this thesis is that employed by Kent *et al.*, (2017):

$$N_v(x) = \frac{(1+\tanh(4x+2))(1-\tanh(4x-2))}{(1+\tanh\,(2))^2}, \tag{3.5}$$

which produces four transverse jets with opposite directions. The initial conditions are $h(x,0)+b(x,0)=1$, $hu(x,0)=hr(x,0)=0$, and $hv(x,0)=N_v(x)$ (Figure 3.3). The height of topography $b(x)$ is zero throughout the domain to simplify the case.

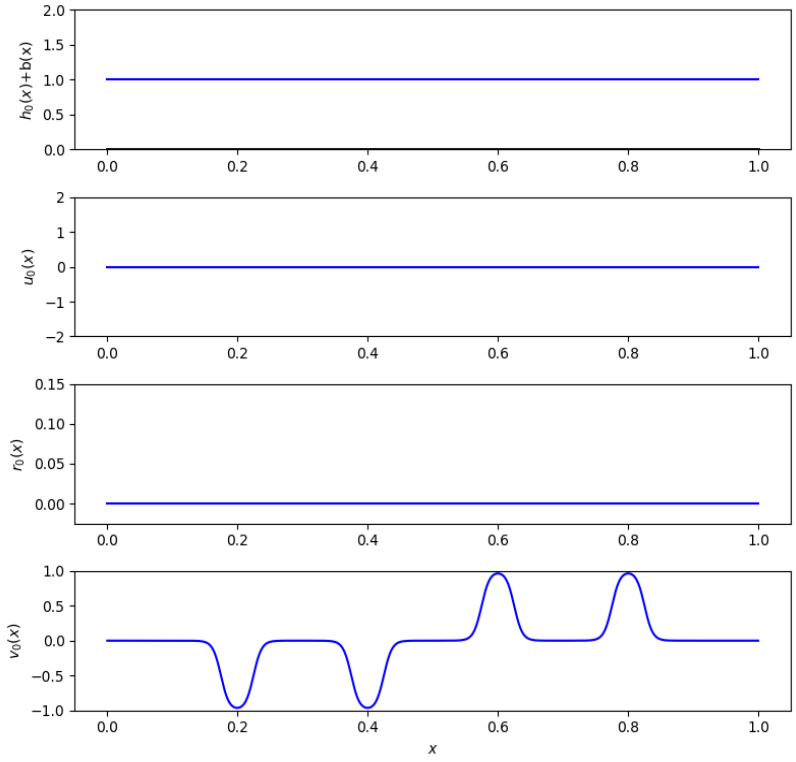

Figure 3.3: The initial conditions of variables in the rotating flow case. From the top to bottom: $h(x)+b(x)$, u(x), $r(x)$, and $v(x)$.

The thesis also considers a case of non-rotating flow over topography. For that case, a superposition of sinusoids is considered as the underlying surface, which is defined as:

$$b(x) = \begin{cases} \sum_{i=1}^{3} b_i, & \text{for } x_p < x < x_p + 0.5 \\ 0, & \text{elsewhere} \end{cases}, \tag{3.6a}$$

$$\text{with } b_i = A_i \left(1 + \cos\left(2\pi\left(k_i\left(x - x_p\right) - 0.5\right)\right)\right), \tag{3.6b}$$

where $x_p = 0.1$, $k = \{2, 4, 6\}$, and $A = \{0.1, 0.05, 0.1\}$. In the non-rotating case, as the transverse velocity v is zero, only three variables are taken into account: h, u, and r, and the flow is purely one-dimensional in space. The initial conditions of these variables are shown in Figure 3.4, where $h(x, 0) + b(x, 0) = 1$, $hu(x, 0) = 1$, and $hr(x, 0) = 0$.

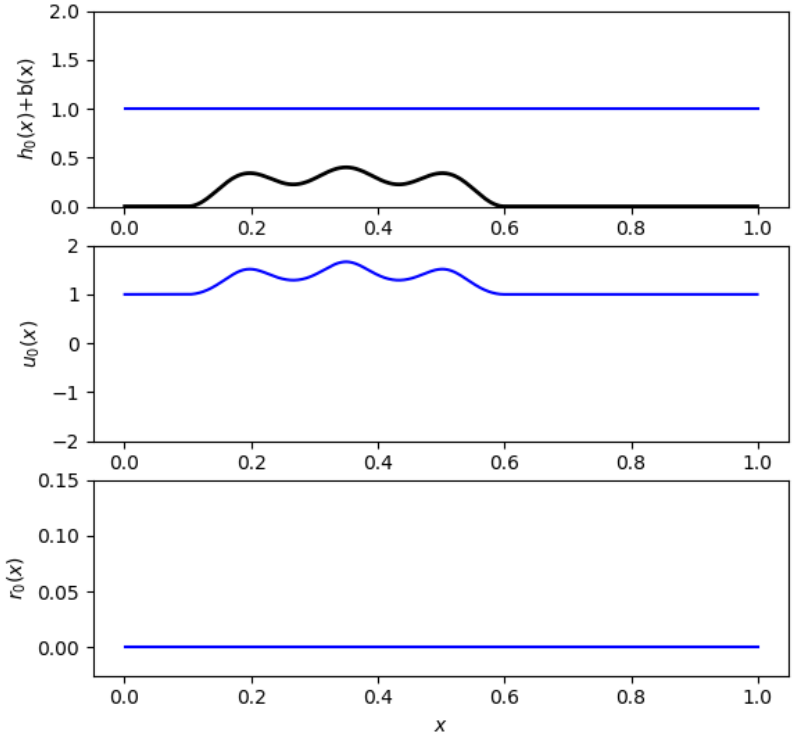

Figure 3.4: The initial conditions of variables in the non-rotating flow case. From the top to bottom: $h(x)+b(x)$, and $r(x)$. The black line in the top panel shows the shape of topography $b(x)$.

A series of numerical experiments based on these two scenarios have been conducted by Kent *et al.,* (2017) and the outputs clearly illustrate aspects of convection and precipitation, highlighting the well-designed dynamics of the model. Also, it has been demonstrated by Kent *et al.,* (2020) that the model provides an idealised testbed for studying the DA system in the presence of convection and precipitation, and hence it provides an approach to investigate the key questions of this project.

3.2 Data assimilation: Ensemble Kalman Filter

Data assimilation is the process of combining imperfect observations with prior knowledge (e.g. previous model forecasts) to obtain a more realistic estimate of the state of the system and the associated uncertainties (Katzfuss *et al.,* 2016). According to Ha and Snyder (2014), the Ensemble Kalman Filter (EnKF) is a sophisticated statistical method of DA that directly extracts the dynamical information from previous forecasts and obtains the weighting of observations and model background via inhomogeneous background error covariances. The EnKF follows the same conceptual

framework as the Kalman filter, however the state distribution is represented by an 'ensemble', which is propagated forward through time and updated when new data is added in. The ensemble representation is a form of dimension reduction, which leads to computational feasibility even for very high-dimensional systems (Katzfuss *et al.*, 2016). Figure 3.5 is an example of ensemble trajectories of forecast, analysis and truth in the model, which shows the basic data assimilation problem: adjusting the forecast via perturbed observations to better estimate the true state.

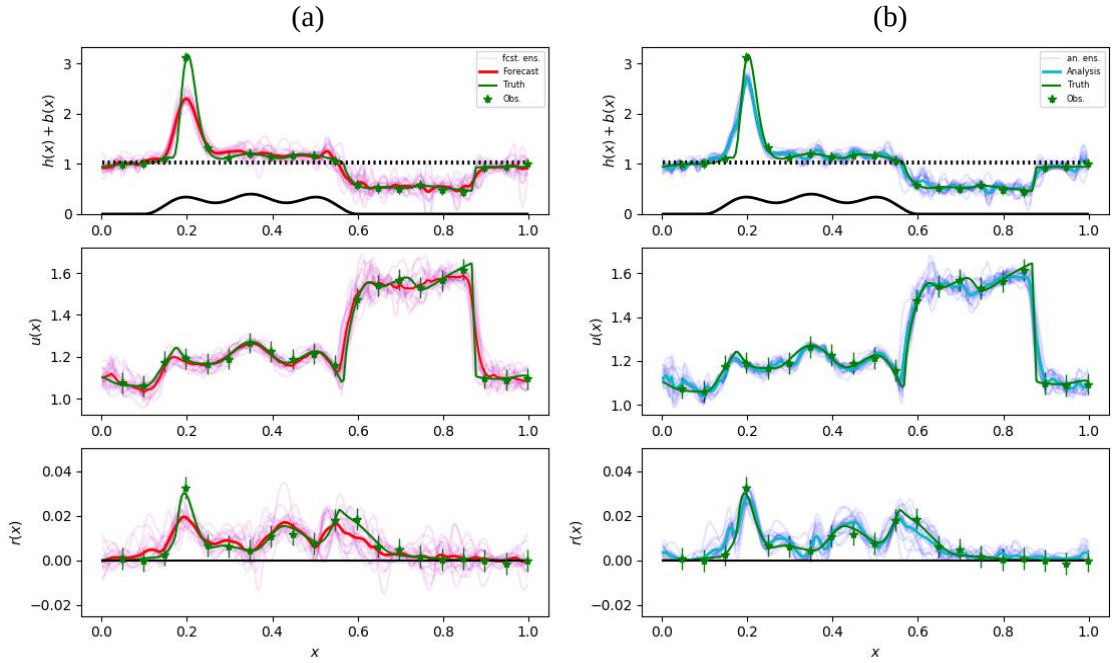

Figure 3.5: An example snapshot of forecast (a), analysis (b) and the truth (green lines) in the non-rotating flow case at t = 0.432 in this project. Only three variables (h+b, u, r) are present. The light pink and blue lines show each ensemble member of the forecast and analysis respectively. The black line in the top panel is topography b and the green dots with error bars are pseudo-observations. The analysis ensemble mean (the bright blue line) shows less discrepancies to the truth than forecast ensemble mean (the bright pink line), indicating the effect of adding observations.

The Monte Carlo approach to EnKF starts from creating a finite number of perturbations to the initial condition, which is the same as the size of ensemble (Stephenson and Doblas-Reyes, 2000). The ensemble attempts to sample the probability density function (pdf) of the true state. As is typical in Monte Carlo approaches, the best estimation of the state in a linear system is present as the ensemble mean $\overline{\boldsymbol{X}}$ which denotes the model state:

$$\overline{\boldsymbol{X}} = \frac{1}{N}\sum_{j=1}^{N} \boldsymbol{X}_j, \tag{3.7}$$

where $\boldsymbol{X}_j$ is the state of the j^{th} member of the ensemble. The forecast error covariance is then calculated through the finite ensemble:

$$\boldsymbol{P}_e^f = \frac{1}{N-1}\sum_{j=1}^{N}(\boldsymbol{X}_j - \overline{\boldsymbol{X}})\,(\boldsymbol{X}_j - \overline{\boldsymbol{X}})^T = \frac{1}{N-1}\boldsymbol{X}\boldsymbol{X}^T, \tag{3.8}$$

where the forecast errors are derived from the perturbations from the ensemble mean rather than the truth.

EnKF consists of a forecast step and an analysis step at each time step. During the forecast step, for an N-member ensemble, the forecast state of the j^{th} member $\boldsymbol{X}_j^f$ at time t_i is determined from the analysis $\boldsymbol{X}_j^a$ at time t_{i-1} as propagated forwards in time with the (imperfect) forecast model $\mathcal{M}$ (see Kent *et al.*, (2017)):

$$\boldsymbol{X}_j^f(t_i) = \mathcal{M}\left[\boldsymbol{X}_j^a(t_{i-1})\right],\ j = 1, \dots, N. \tag{3.9}$$

Then, in the analysis step, observations are merged with information from the previous forecast step to give a best estimation (analysis state) of the truth. In this step, a randomly perturbed observational vector $\boldsymbol{y}_j$ at t_i is assimilated into the system, yielding the analysis state at t_i:

$$\boldsymbol{X}_j^a(t_i) = \boldsymbol{X}_j^f(t_i) + \boldsymbol{K}_i\left(\boldsymbol{y}_j - \boldsymbol{H}_i\boldsymbol{X}_j^f(t_i)\right), \tag{3.10}$$

$$\boldsymbol{K}_i = \boldsymbol{P}_i^f\boldsymbol{H}_i^T(\boldsymbol{H}_i\boldsymbol{P}_i^f\boldsymbol{H}_i^T + \boldsymbol{R})^{-1}, \tag{3.11}$$

where $\boldsymbol{K}_i$ is the Kalman Gain matrix, representing the weight of observations to the analysis, $\boldsymbol{P}_i^f$ is the forecast error covariance matrix updated through the Monte Carlo method during the i^{th} cycle of DA, and $\boldsymbol{H}_i$ is the linear observation operator, which maps from model space to observational space to allow direct comparison between the two. The analysis error covariance $\boldsymbol{P}_i^a$ is linked to $\boldsymbol{P}_i^f$ through an identity matrix $\boldsymbol{I}$, the gain matrix $\boldsymbol{K}_i$ and the linear observation operator $\boldsymbol{H}_i$:

$$\boldsymbol{P}_i^a = (\boldsymbol{I} - \boldsymbol{K}_i \boldsymbol{H}_i)\boldsymbol{P}_i^f, \tag{3.12}$$

As for a stochastic update, the observations are treated as a perturbed ensemble as:

$$\boldsymbol{y}_j = \boldsymbol{y} + \boldsymbol{\epsilon}_j^o, \quad \boldsymbol{\epsilon}_j^o \sim \mathcal{N}(0, \boldsymbol{R}), \tag{3.13}$$

where the distribution of the observational vector $\boldsymbol{y}_j$ has the mean equal to the measured observation $\boldsymbol{y}$ and the error $\boldsymbol{\epsilon}_j^o$ following a Gaussian distribution with covariance matrix $\boldsymbol{R}$. $\boldsymbol{R}$ is chosen to represent the uncertainty in the observations, which includes instrument error and uncertainty in the observation operator.

It is worth mentioning that according to Stephenson and Doblas-Reyes (2000), an ensemble with finite size is likely to converge slowly and to under-sample the true pdf of the atmospheric state particularly when the number of degrees of freedom of the model is much larger. Hence, the Monte-Carlo nature of EnKF could lead to sampling error since there are finite number of ensemble members in the forecast model $\mathcal{M}$, typically at 10 to 100, which is much smaller than the number of degree of freedom in the model (Kent *et al.*, 2020). Ensemble inflation techniques are applied to mitigate the problems caused by under-sampling, attempting to maintain a sufficient ensemble spread, for example by artificially adding random Gaussian perturbations $\eta_j \sim \mathcal{N}(0, \gamma_a^2 \boldsymbol{Q})$ during the forecast step (Eq 3.9):

$$\boldsymbol{X}_j^f(t_i) = \mathcal{M}\left[\boldsymbol{X}_j^a(t_i - 1)\right] + \eta_j, \; j = 1, \ldots, N, \tag{3.14}$$

where the model error matrix $\boldsymbol{Q}$ is prescribed from some knowledge of the modelling system and γ_a is a tuneable parameter controlling the overall magnitude of the sample perturbations (Kent *et al.*, 2017).

Ensemble error and spread

The accuracy of ensemble performance can be quantified by the root mean square error (RMSE) of the ensemble as well as the ensemble spread (SPR). They can be computed either for the for the forecast or the analysis so that the ensemble at both stages can be verified. The RMSE is defined as:

$$RMSE = \sqrt{\frac{1}{n}\sum_{k=1}^{n}(\bar{x}_k - x_k^t)^2}, \text{ where } \bar{x}_k = \frac{1}{N}\sum_{j=1}^{N} x_{k,j}, \quad (3.15)$$

and $\bar{x}_k$ can be the ensemble mean of the kth component of either the analysis or the forecast vector, and x_k^t is the kth component in the truth (the nature run) vector $\boldsymbol{x}^t$. In addition, the SPR among ensemble members is derived from the root mean square difference between the ensemble mean and ensemble members, which for the forecast can be expressed as:

$$SPR\_fc = \sqrt{\frac{1}{N-1}\sum_{j=1}^{N}\frac{1}{n}\sum_{k=1}^{n}(x_{k,j} - \bar{x}_k)^2} \equiv \sqrt{\frac{1}{n}Tr\left(P_e^f\right)}, \quad (3.16)$$

where the Tr (P_e^f) means the trace of the forecast error covariance matrix, calculated by the sum of the diagonal values, and $x_{k,j}$ denotes the forecast vector. Similarly, for the analysis:

$$SPR\_an = \sqrt{\frac{1}{N-1}\sum_{j=1}^{N}\frac{1}{n}\sum_{k=1}^{n}(x_{k,j} - \bar{x}_k)^2} \equiv \sqrt{\frac{1}{n}Tr(P_e^a)}, \quad (3.17)$$

where $x_{k,j}$ is from the analysis vector, and P_e^a is the analysis error covariance matrix. Comparison of the SPR and RMSE statistics provides a simple but important diagnostic on the reliability and suitability of the generated ensemble in the EnKF (Kent *et al.*, 2020): the magnitude of SPR of an ideal ensemble is expected to be the same as the RMSE at the same lead time in order to adequately represent the uncertainty during the forecast (Stephenson and Doblas-Reyes, 2000). Since the study focuses on the observational influence on analysis, the RMSE and SPR of analysis will be compared for evaluating the sufficiency of spread of analysis ensemble after assimilating the observations in Section 5.

3.3 Quantifying the value of observations

Approaches have been derived to evaluate the value of observations in DA schemes for the better understanding of the DA system itself (Baker and Daley, 2000; Cardinali *et al.*, 2004). These techniques attempt to quantify the partition of the influence assigned to the observations and the background respectively, as well as the amount of information extracted by all the available data or specific types of observations. In this

project, the observational influence matrix developed from Cardinali *et al.*, (2004) is applied to assess the value of observation.

3.3.1 Classical statistical definitions of influence matrix and self-sensitivity

The method is based on the idea that in least-squares (LS) regression, any change in observation $\boldsymbol{y}_i$ gives a proportional effect on the corresponding predicted value $\widehat{\boldsymbol{y}}_i$, which is expressed as the linear combination of observed $\boldsymbol{y}_i$ (Velleman and Welsh, 1981). For an ordinary linear regression model, the response of predicted vector $\hat{\mathbf{y}}$ to observational vector $\mathbf{y}$ can be written as:

$$\hat{\mathbf{y}} = \mathbf{S}\mathbf{y}, \tag{3.18}$$

where $\mathbf{S}$ is the influence matrix, denoting the rate of change of $\hat{\mathbf{y}}$ with respect to variations of $\mathbf{y}$. Thus, it can be easily derived that:

$$\mathbf{S} = \frac{\partial \hat{\mathbf{y}}}{\partial \mathbf{y}} \tag{3.19}$$

and the off-diagonal ($i \neq j$) and diagonal ($i = j$) elements are thus:

$$\begin{aligned} S_{ij} &= \frac{\partial \hat{\mathrm{y}}_j}{\partial \mathrm{y}_i}, \\ S_{ii} &= \frac{\partial \hat{\mathrm{y}}_i}{\partial \mathrm{y}_i}, \end{aligned} \tag{3.20}$$

where the i^{th} diagonal element S_{ii} measures the self-sensitivity of $\hat{\mathrm{y}}_i$ to y_i at the same data point, whereas the off-diagonal elements denote the cross-sensitivity between two data points. It is discussed by Hoaglin and Welsh (1978) that the diagonal elements satisfy:

$$0 \leq S_{ii} \leq 1 \tag{3.21}$$

with zero self-sensitivities ($S_{ii} = 0$) implying no influence of observations to the analysis, while $S_{ii} = 1$ indicating that the analysis at that data point is entirely determined by the observations.

3.3.2 Observational influence and self-sensitivity for a DA scheme

The analysis step in the EnKF provides an optimal analysis state $\mathbf{x}^a$ (the ensemble mean of $\boldsymbol{X}_j^a$ in Eq 3.10) by combining the observations y with the forecast state $\mathbf{x}^f$ (the ensemble mean of $\boldsymbol{X}_j^f$ in Eq 3.10):

$$\begin{aligned} \mathbf{x}^{\mathrm{a}} &= \mathbf{x}^{\mathrm{f}} + \mathbf{K}\left(\mathbf{y} - \mathbf{H}\mathbf{x}^{\mathrm{f}}\right) \\ &= \mathbf{K}\mathbf{y} + (\mathbf{I} - \mathbf{K}\mathbf{H})\mathbf{x}^{\mathrm{f}}, \end{aligned} \tag{3.22}$$

where the gain matrix $\mathbf{K} = \mathbf{P}^{\mathrm{f}}\mathbf{H}^{\mathrm{f}}(\mathbf{H}\mathbf{P}^{\mathrm{f}}\mathbf{H}^{\mathrm{T}} + \mathbf{R})^{-1}$ contains the information on the respective accuracies of observations (observational error covariance matrix $\mathbf{R}$) and of the forecast (forecast error covariance matrix $\mathbf{P}^{\mathrm{f}}$), and $\mathbf{I}$ is an identity matrix. The analysis state interpolated into observational space is then:

$$\hat{\mathbf{y}} = \mathbf{H}\mathbf{x}^{\mathrm{a}} = \mathbf{H}\mathbf{K}\mathbf{y} + (\mathbf{I} - \mathbf{H}\mathbf{K})\mathbf{H}\mathbf{x}^{\mathrm{f}}, \tag{3.23}$$

with the observations and the background information weighted by $\mathbf{HK}$ and $\mathbf{I} - \mathbf{HK}$ respectively. From Eqs 3.23 and 3.19, the analysis sensitivity with respect to observations is written as:

$$\mathbf{S} = \frac{\partial \hat{\mathbf{y}}}{\partial \mathbf{y}} = \mathbf{H}\mathbf{K}. \tag{3.24}$$

Similarly, the analysis sensitivity with respect to the background information (in observation space) is thus:

$$\frac{\partial \hat{\mathbf{y}}}{\partial (\mathbf{H}\mathbf{x}^{\mathrm{f}})} = \mathbf{I} - \mathbf{H}\mathbf{K} = \mathbf{I} - \mathbf{S}. \tag{3.25}$$

Eqs 3.24 and 3.25 indicate that the observational influence on the analysis is complemented by the background influence. For example, if the analysis sensitivity with respect to the i^{th} observation is S_{ii}, then the influence of background information at same location and time will simply be 1-S_{ii}.

Figure 3.6 shows an example of the sensitivity matrix S from a snapshot in the simulation of the rotating flow case. Clearly, as for the four diagonal sub-matrices, the high values are highly centralised along the diagonals, implying that the self-sensitivities are much important than the cross-sensitivities. Hence, the self-sensitivity of each variable is a key point to investigate in this thesis. The off-diagonal elements and the other sub-matrices represent the analysis sensitivity of one variable to another and show how the observational influence can spread further. This also indicates an interesting direction of research. Note that since different observations can have different units, the cross-sensitivities have the units of the corresponding unit ratios. Hence the cross-sensitivities of different pairs of observations are not directly comparable. However, self-sensitivities are pure numbers (no units) as in standard regression (Cardinali *et al.*, 2004).

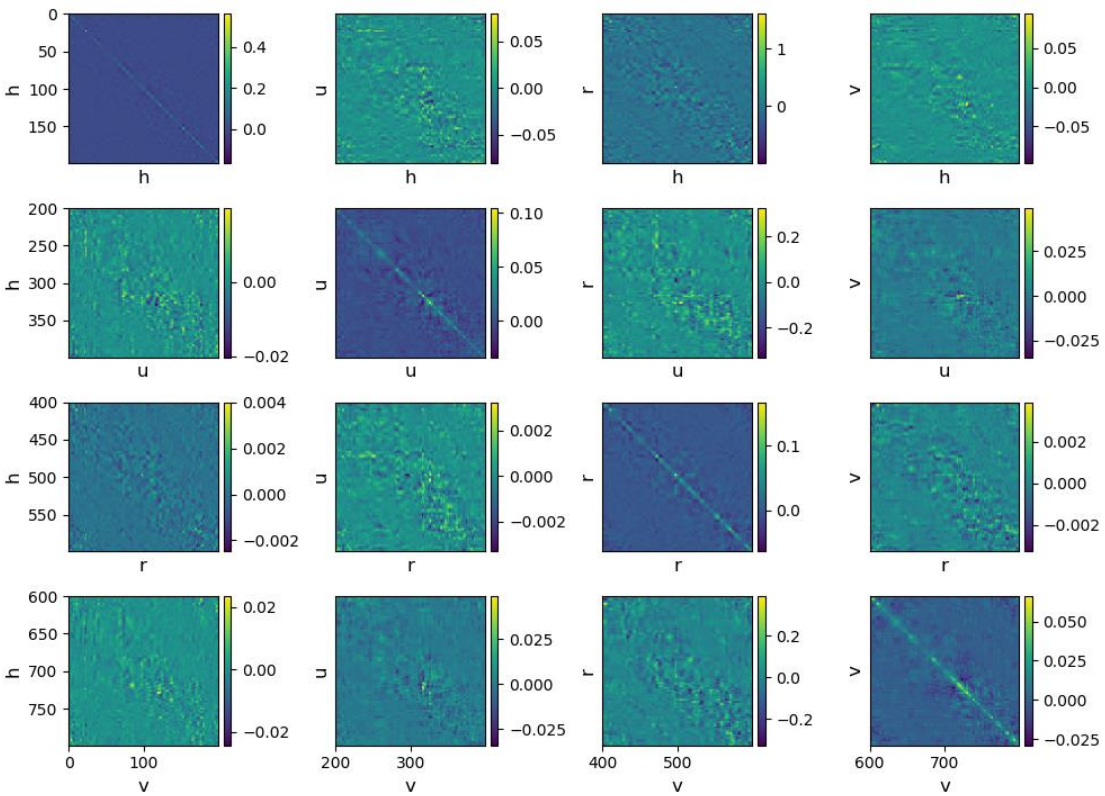

Figure 3.6: An example sensitivity matrix S of the rotating flow case at t=0.432. The vertical and horizontal coordinates are the elements of the observations over the domain. The variables at vertical and horizontal coordinates represent the analysis and the observations respectively. The variables are observed each 2.5 km so there are total 800 elements for 4 variables given that the domain length is 500 km.

The global average observation influence diagnostic is defined as:

$$OID = \frac{\mathrm{Tr}(\mathbf{S})}{p}, \tag{3.26}$$

where the overall influence of all the observations is normalised by the total number of observations (p). Cardinali *et al.*, (2004) applied this diagnostic to ECMWF global NWP model and finds that the overall influence of observations is not very high (*OID* = 0.15), which means the observations actually act as an adjustment to the prior forecasts rather than completely replacing them. This is attributed to the fact that observations are too sparse and incomplete to describe the whole picture of the state, compared to the model system. Nevertheless, it should be noted that the model forecasts also contain the observational information from previous DA cycles.

Moreover, Partial Influence (PAI) is another index of interest that measures the observation influence for any subset of data:

$$PAI = \frac{\sum_{i \in I} S_{ii}}{p_I}, \tag{3.27}$$

where the subset *I* can be a particular observation type, a specific horizontal or vertical domain, or a specific meteorological variable, and p_I is the number of data in *I*. In this project, the PAI of variables involved in the idealised fluid model (*h, u, r, v*) will be analysed.

Chapter 4

Experimental design and set-up

The following research of observational influence in the DA process is carried out via a so-called 'twin experiment' setting, where the model mainly generates three trajectories: model forecast which is totally determined by the background information, model analysis which is the production after assimilating the observations, and a nature run which can be seen as a synthetic truth. To mimic an operational DA process, the experiments are performed in an 'imperfect' model scenario, which means the forecasts are generated using a worse model configuration, such as with less well-specified model parameters or at lower resolutions (Kent *et al.,* 2017). Furthermore, pseudo-observations are created from the truth simulation with a specified error distribution before being assimilated into the forecast model at each DA cycle to produce model analysis. This setting allows the comparisons between the model analysis and forecast, and the truth. Also, it links the observational influence on the analysis to the real accuracy of analysis, providing a way for evaluating whether the influence is useful or not. In this chapter, the construction of the twin experiments will be described in detail, including the experimental design and the set-up of parameters.

4.1 Experimental design

The major question to be solved in this project, as proposed in Section 1.2, contains the following aspects:

1. The questions on the factors that control the influence of the observations:
    a. How does the influence of the observations depend on the presence of convection?
    b. How does the density of the observations affect the influence? Can an optimal density be found?
    c. How does the observational information propagate in space and to different model variables?
2. How does the observation influence correspond to the accuracy of the analysis? Does each observation give optimal influence on the forecast?

The experiments designed to investigate the above questions are conducted for both scenarios (non-rotating and rotating case). In order to test the observational influence in different environmental conditions (question a), the self-sensitivities (diagonals of **HK** matrix) at each grid point will be compared with the weather conditions at the same locations. Also, the PAI (Eq 3.27) and the overall observational influence (OID in Eq 3.26) will be calculated under different observational densities (see Obs. density in Table 4.1) for question b. As for question c, the cross sensitivity among different variables will be investigated in order to find if the observations of one variable can influence the analysis of other variables. The experiment to accomplish this is to remove the observations of one or two specific variables and see how the rest of the observed variables would help to forecast the un-observed variables, which might give insights to 'data thinning' of real observations. Additionally, a high influence does not always guarantee a useful influence. To investigate this point, the RMSE (Eq 3.15) and SPR (Eq 3.17) of analysis will be applied to link the observational influence on the accuracy of the analysis. SPR shows the accuracy estimated by the analysis, based on the agreement of each ensemble member, while RMSE indicates the true accuracy of the analysis compared to the truth. A consistency between the two implies whether the observations are given the right weight in assimilation. Therefore, as mentioned in Section 3.2, RMSE and SPR should have the same magnitude for an optimal ensemble performance.

4.2 Setting up an idealised forecast-assimilation system

Currently, most operational high-resolution NWP models are equipped with fine horizontal grid spaces on the order of 1 km, due to which the convective-scale phenomena are simulated explicitly (Lean *et al.*, 2008). With this in mind, the forecast grid size is set at ~2.5 km in this fluid model. Hence, given that the length of domain is $L_0 = 500$ km, the computational grid of each variable contains $N_{el} = 200$ elements. Nevertheless, it is recognised that convective activities are still under-resolved even in the models with such resolutions (Tang *et al.*, 2013). This deficiency of the model forecast is reflected in the twin experiments through generating the nature run with the resolution 4 times finer than the forecast model ($N_{el} = 800$ for the nature run). As shown in Figure 4.1, the forecast trajectories are smoother with un-resolved convective features while the truth shows sharper and more resolved convections and precipitations.

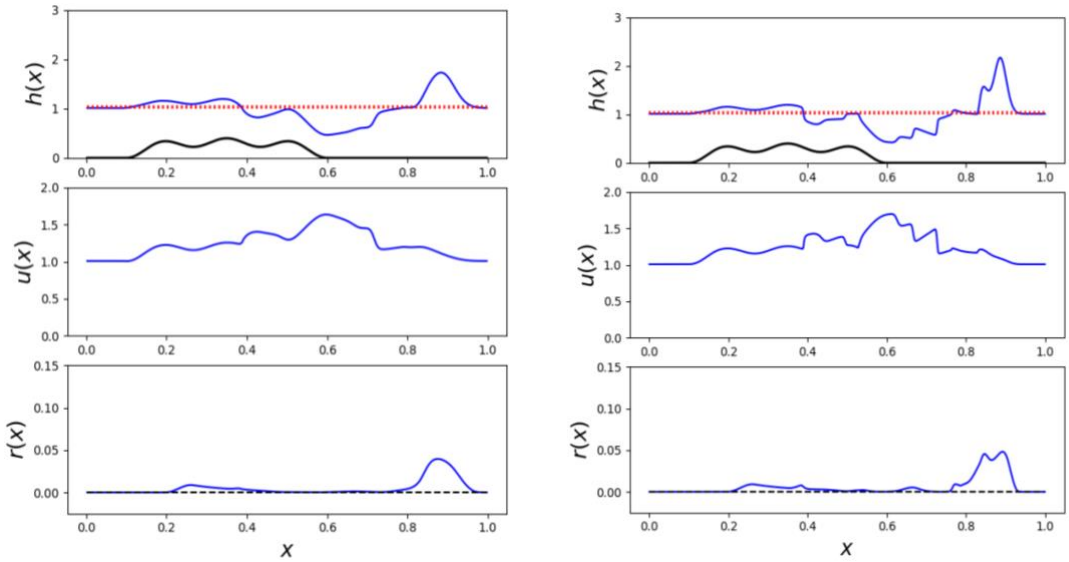

(a) Forecast $\mathbf{x}^f$: $N_{el} = 200$ (b) Nature run $\mathbf{x}^t$: $N_{el} = 800$

Figure 4.1: The example forecast trajectory (a) and the nature run (b) of model variables *h* (top), *u* (middle), and *r* (bottom) of non-rotating scenario at t = 0.432. The red dotted lines are the thresholds for convections and precipitation.

To further aid the realism of the experiments, Kent *et al.*, (2017) adopts the Rossby number (R_o) and the Froude number (F_r) into the non-dimensional SWEs in order to achieve the comparison between quantities with different physical units. These two non-dimensional parameters describe the relative strength of rotation and fluid stratification compared to advection, and are expressed as below:

$$R_o = \frac{V_0}{fL_0}, \quad F_r = \frac{V_0}{\sqrt{gH_0}}, \tag{4.1}$$

where V_0, L_0, and H_0 are characteristic scales of velocity, domain length and height, with the typical values at 20 m/s, 500 km, and 500 m in this model. Large values of Rossby number indicates non-rotating flow when Coriolis parameter f is extremely small. We will consider two cases: one where the Rossby number is set to be infinite for non-rotating flow, and another where it is small (0.1) for rotating flow. Moreover, given that the domain length $L_0 = 500$ km and velocity scale $V_0 = 20$ m/s, the time scale for advection through the domain T_0 is at ~25000 s, equals to ~6.94 hours. One hour is thus equal to ~0.144 non-dimensional time units.

Another key issue in DA experiments is the set-up of the initial ensemble ($\boldsymbol{X}_j^a(t_0)$ in Eq 3.10). As noted in Evensen (2007), the initial ensemble is supposed to cover as fully as possible the initial uncertainties of the model state. The ensemble is initiated with spatially uncorrelated random Gaussian perturbations (Zhang *et al.*, 2004), which are then allowed to spin-up so that they exhibit the dynamical structure of the errors in the model (Houtekamer and Zhang, 2016). As such, a set of initial errors $\boldsymbol{\sigma}^{ic} = \left(\boldsymbol{\sigma}_h^{ic}, \boldsymbol{\sigma}_{hu}^{ic}, \boldsymbol{\sigma}_{hr}^{ic}\right) = (0.1, 0.005, 0)$ is used to generate the initial ensemble for twin experiments here. The initially perturbed ensemble is thus:

$$h_j(x,0) = h(x,0) + \sigma_h^{ic} z_j, j = 1, \ldots, N, \quad \text{where } z_j \sim N(0,1), \tag{4.2}$$

where $h(x,0)$ represents the initial fluid depth, and similarly for *hu* and *hr*. The subscript j the denote the spatial point. Note that the initial uncertainty for *r* variable is zero since the initial rain field is zero everywhere. Observations are then assimilated hourly over a 20-hour period, with a specific error $\boldsymbol{\sigma} = (\sigma_h, \sigma_u, \sigma_r, \sigma_v)$ (see Table 4.2). The set-up of the experiments is based on the well-tuned parameters for experiments conducted in Kent *et al.*, (2017) and Kent *et al.*, (2020). Table 4.1 provides an overview of parameters used in the model and DA cycles (see Kent *et al.*, (2020) for detail).

Model parameters		Filter parameters	
Rossby number, R_o (non-rotating/rotating)	∞/0.1		
Froud number, F_r	1.1	Update frequency, *dt* [hr]	1
Boundary conditions	Periodic	Ensemble size, *N*	18
Velocity scale V_0 [ms^{-1}]	20	Number of DA cycles	20
Height scale H_0 [m]	500	Obs. error	(0.1, 0.05, 0.005,
Domain length, L_0 [km]	500	$(\sigma_h, \sigma_u, \sigma_r, \sigma_v)$	0.05)
Forecast N_{el},	200	Obs. density, d [km]	(2.5, 5, 10, 25, 50)
Nature run N_{el}^t,	800	Initial ensemble	(0.05, 0.05, 0.0,
Convection threshold, H_c	1.02	perturbations	0.05)
Precipitation threshold, H_r	1.05	$(\sigma_h^{ic}, \sigma_{hu}^{ic}, \sigma_{hr}^{ic}, \sigma_{hv}^{ic})$	
α	10		
β	0.2		
${c_0}^2$	0.085		

Table 4.1: An overview of the model and assimilation parameters used in the twin experiments.

Chapter 5

The value of observations

This chapter displays the results corresponding to the specific questions proposed in Chapter 4 in detail, including the dynamics in both scenarios (rotating flow and non-rotating flow over topography), variations of observational influence in the presence of convection and with different observational densities, and the linkage of observational influence to the accuracy of the analysis.

5.1 Rotating flow

Within this section I explore the Rossby adjustment scenario where the fluid surface is disturbed from its initial constant height when adding a perturbation to the transverse velocity $v(x)$. Figure 5.1 is the snapshot of the time evolution of free surface height, wind convergence, the rainfall, and the gradient of transverse velocity. It can be seen that the disturbance of v would cause perturbations in the other three fields from their calm initial conditions, and these perturbations oscillate throughout time. The production of the rain mass $r(x)$ corresponds to the exceedance of precipitation threshold (H_r in Table 4.2), and to positive wind convergence $-\partial_x u$. The horizontal wind shear of transverse velocity $-\partial_x v$ is shown in order to illustrate ageostrophic conditions, and this is discussed shortly. The perturbations initiate slightly left to the locations of the initial negative jet and to the right of the positive jet, before generally propagating to both sides and getting weakened through time, implying the Rossby adjustment of fluid height to the initial disturbance in the model.

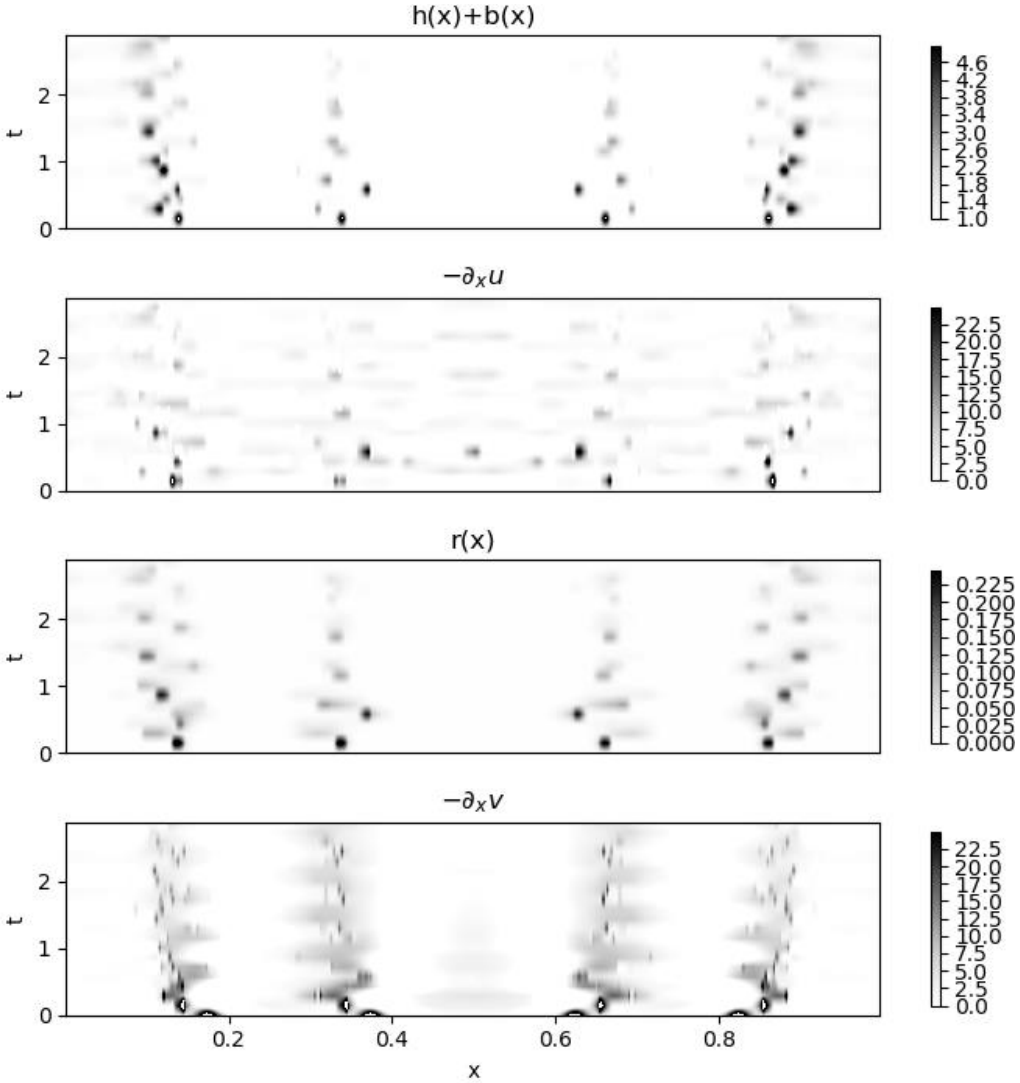

Figure 5.1: Hovmoller plot for rotating flow, highlighting the condition for initiation and the subsequent evolution of convection. From the top to bottom: $h(x)+b(x)$, $-\partial_x u$, $r(x)$, and $-\partial_x v$.

Shallow water flow in perfect geostrophic balance between the pressure gradient and rotation satisfies the equation below:

$$g\partial_x h - fv = 0 \text{ and } u = 0. \tag{5.1}$$

The difference between large-scale and convective-scale NWP is in some sense the difference between balanced and unbalanced dynamics. As for a traditional NWP model which focuses on synoptic scale phenomena, its DA system is based on geostrophic and hydrostatic balance. However, these balances are no longer feasible at convective scales, as vertical accelerations become increasingly significant in the flow.

Thus, there is an interesting point in this modRSW model: it captures the breakdown of these large-scale balances (Kent *et al.*, 2017).

Theoretically, due to the construction of effective pressure term (Eq 3.3a) and its gradient (Eq 3.3b), a disruption of the balance is expected to occur where convections happen. The top panel of Figure 5.2 is the real exceedance of convective threshold from the nature run, illustrating when and where the convection happens. The second and third panels plot the difference (Eq 5.1) derived from the nature run and model analysis respectively as a function of time and space. From the top two panels, the locations where the state is close to geostrophic balance or where this balance is broke are consistent with the occurrence of convections. Also, with the weakening of convections through time, the departure from geostrophic balance correspondingly becomes smaller and finally close to the balance, which again demonstrates the Rossby adjustment theory above.

By comparing the result from the nature run (middle) and the model analysis (bottom), the DA process is helpful to fix the locations of breakdowns of geostrophic balance during the first few assimilation cycles, whereas the magnitude of each breakdown is much smaller than that of nature run, and many weak breakdowns during the second half period cannot be well resolved. Bannister, Migliorini and Dixon, (2011) attributes the geostrophic balance decays to the decrease in horizontal scale, which is also suitable to explain the difference here. The model generates its truth with a total number of grid points N_{el} = 800 through the domain while the analysis only has 200 elements, and the cores of the convections only occupy a few grid points across even in high resolution cases. Hence, the physical length of the convection at N_{el} = 800 cannot be resolved properly with N_{el} = 200, which affects the horizontal pressure gradient $\partial_x h$. Thus, it is reasonable that instead of a very peaked departure in the truth, the analysis produces a weaker departure over a larger physical length. The example here verifies the ability of modRSW model in exhibiting the desirable feature of Rossby adjustment dynamics where the flow is far from the geostrophic balance in the presence of convections and precipitations whilst remaining close to balance in non-convective regions, and thus the model is feasible for the subsequent DA experiments on investigating the influence of observations.

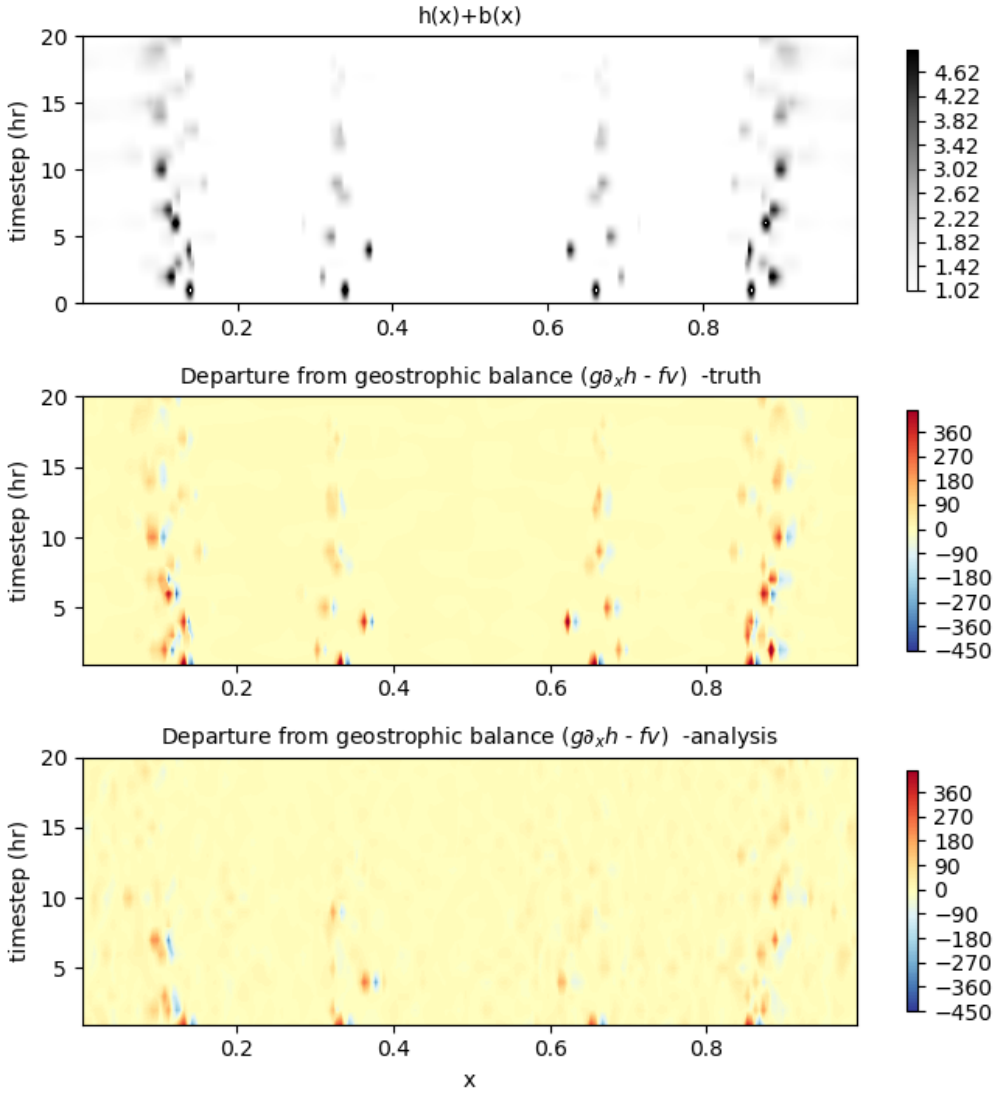

Figure 5.2: Hovmoller plot of time evolution of free surface height (top), and the departure from geostrophic balance ($g\partial_x h - fv$) calculated from nature run (middle) and the model analysis with observational density at 2.5km (bottom).

5.1.1 Analysis sensitivity to observations

In order to find the relationship between the observational influence and the presence of convection, the self-sensitivities of each variable are extracted from each timestep and is exhibited in the right column of Figure 5.3. The comparison between the two columns in Figure 5.3 shows certain consistency between the locations of convection and the locations of large magnitudes of self-sensitivity of pressure and rain mass from the first and the third panels. Here note that the variation of h can in a sense represent the variation of pressure since it constructs the effective pressure term (Eq 3.3a).

Particularly, it can be seen from the rainfall panel that at each timestep, the observation of rain strongly affects its analysis in the vicinity of precipitation. This influence increases when getting close to the convective cores (e.g. for the rainfall at timestep ~ 4 and x ~ 0.4, the observational influence reaches up to 50 %), and keeps higher than the surrounded steady regions throughout the lifetime of convections.

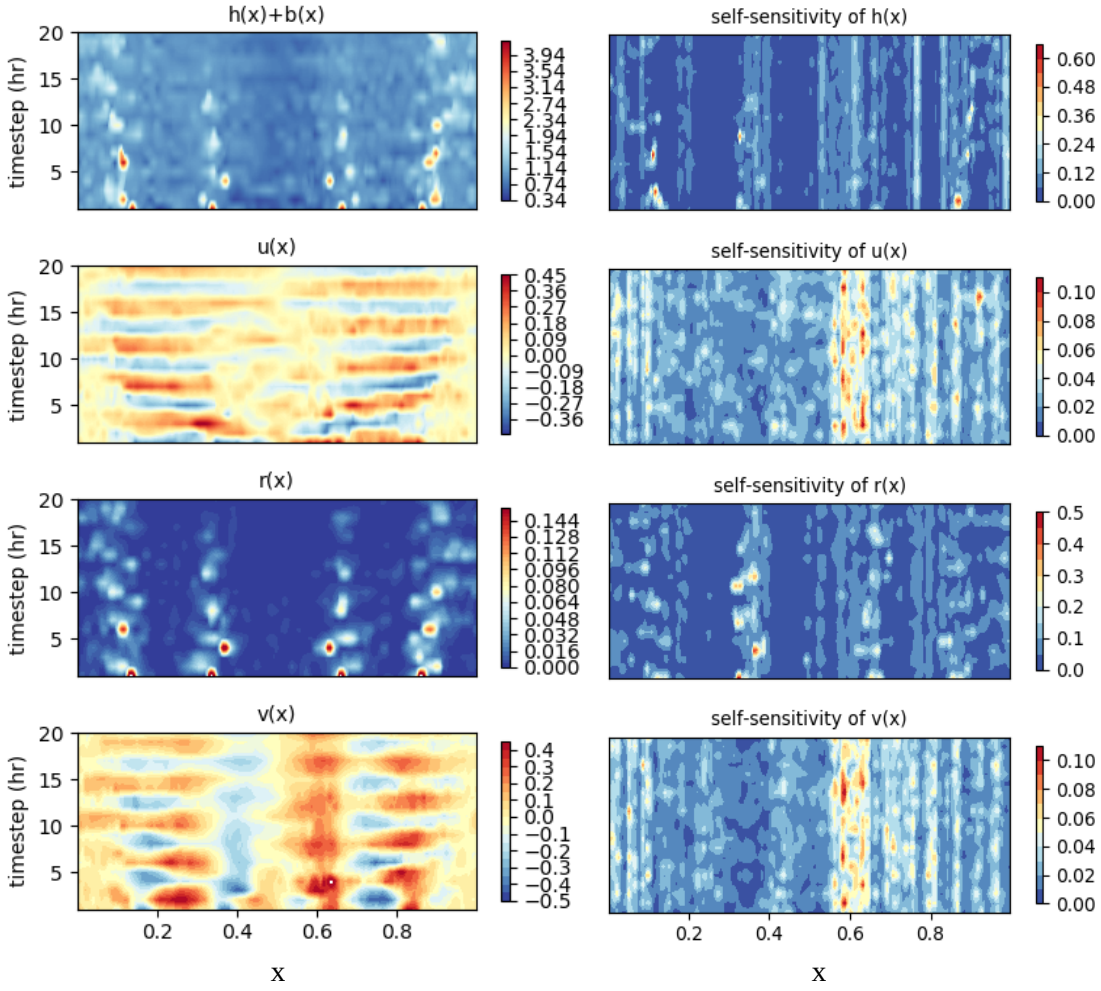

Figure 5.3: Hovmoller plot of the evolution of convections in the model analysis (left column) and the self-sensitivity of each variable (right column) over 20 DA cycles. The variables are observed each 2.5 km.

As for those steady regions, however, the observational influence of both variables can be very weak. Cardinali *et al.*, (2004) conducted experiments investigating the global influence of surface pressure and aircraft wind observations and found that in dynamically active regions (i.e. North Atlantic in their experiment), both types of observation have a large influence on analysis. The behavior of pressure and rainfall

observations here corresponds with the result in Cardinali *et al.*, (2004), while the wind fields exhibit a quite different picture, in which the bright bands of strong self-sensitivities of $u(x)$ and $v(x)$ show little relevance to the evolution of winds or the convection, indicating that the impact of wind observations in DA seems not relevant to the location of convective activities. Also, there are bands of strong influence away from the convective regions in pressure and rainfall fields, and the observational influence for convections with similar magnitudes can vary. Hence, although the observations seem more valuable near convective regions, the observational influence is not entirely determined by the convections.

5.1.2 Effect of the density of observations

What might also affect the performance of observations in DA system, and which observation are most informative in rotating flow? OID (Eq 3.26) are PAI (Eq 3.27) are appropriate diagnostics to quantify the overall influence of the whole observing system and the partial influence of each observed variable. The model is run throughout a 20-hour DA period with observational densities varying from 2.5 km to 100 km. Figure 5.4 illustrates the PAI of each variable and the OID at each observational density, from which we see that the order of the importance of observing the different variables is robust as the density is reduced: the observation of pressure is most valuable with the largest PAI (6 % to 28 %), followed by the observation of rainfall (5 % to 24 %) and the winds (2.5 % to ~23 %) (here we only consider the density below 100 km, although the influences of observation of winds might change the order at even lower densities according to their trends). Moreover, the overall influence of observations (OID) shows a range from 4 % to 25 %. This is comparable to the OID of 15% calculated by Cardinali *et al.*, (2004) in the ECMWF's global DA system.

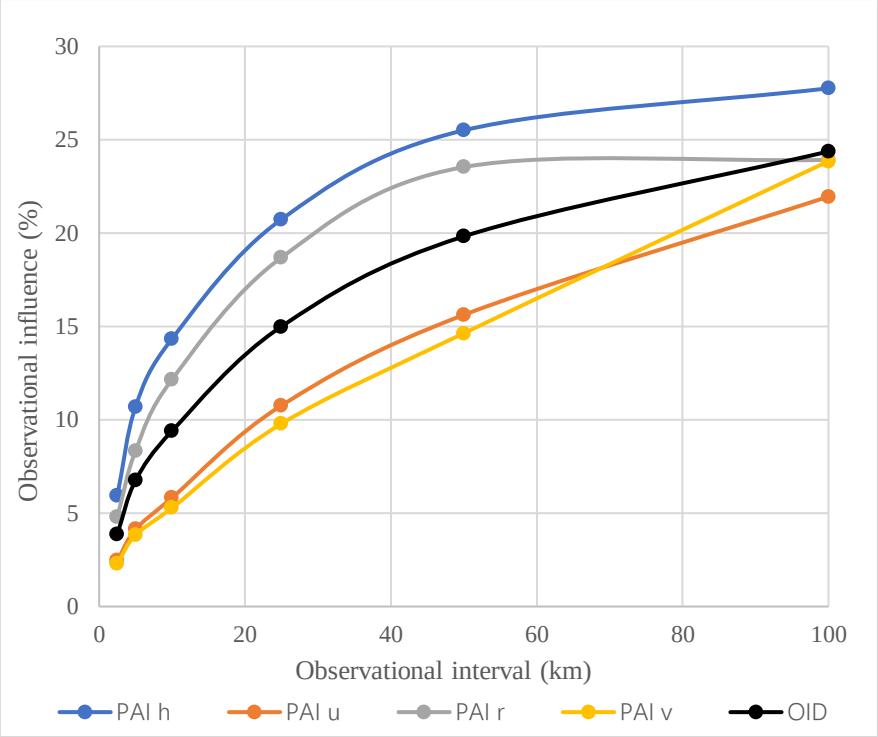

Figure 5.4: The PAI of each variable and OID of the observational system at different observational densities.

Furthermore, from the figure, the observational influence increases parabolically with the reduction of observational density, which is also similar to the result from Cardinali *et al.*, (2004) that low-influence observations usually occur in data-dense areas while high-influence observations are in data-sparse regions. This can be explained by the idea of 'data redundancy' that in practical NWP systems, the observations within a grid cell could either contain the overlapping information from various observing instruments, or contain different information that presumably represents some sub-grid processes that cannot be resolved by the model (Oke *et al.*, 2008). In this experiment, the information in the observation is spread in space and to the other variables via correlations in the forecast ensemble. The information will overlap if two observations are close to each other, leading to the reduction of the influence of both observations.

Figure 5.5 shows an example of the spread of information along grid points for the variable v: the observations are of greatest importance to the analysis at corresponding grid points, but they also propagate information to the adjacent grid points. As the observations become sparser, the influences spread further with increasing magnitudes,

indicating that the decrease in data density will lead to the further spatial spread of observational information, as well as the rise in influence of individual observation at each grid point.

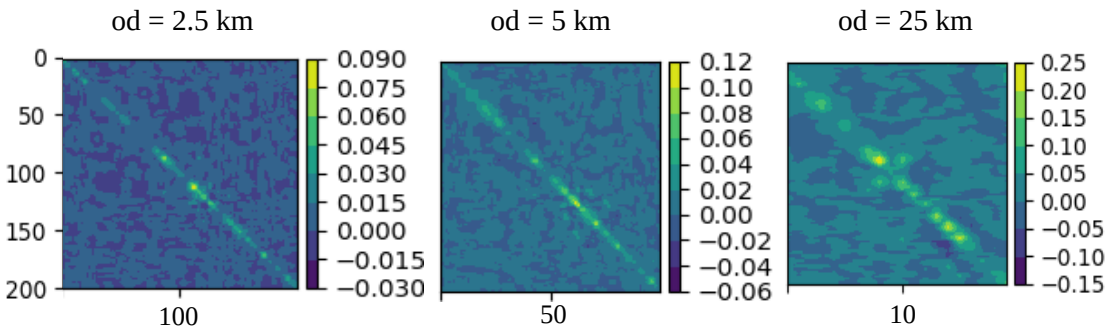

Figure 5.5: The example v component of the K matrix, the sensitivity of the analysis of v (y axis) to observations of v (x axis), with different observational density (od) at 2.5 km (left), 5 km (middle) and 25 km (right) at t = 0.432. For the K matrix, the x axis denotes the observation space depending on the observation density, which is different with the number of grid points of model analysis on the y axis.

The difference of the information spread in wind fields and in *h* and *r* is a possible cause for the divergence of PAI lines between winds and *h* (and *r*) in Figure 5.4. The winds have broader features than convections and precipitations (see the evolution plots in Figure 5.3), which would result in long-range correlations in the ensemble, so that the spread of observational information is expected to be further in wind fields. When increasing the observational density, observations with a larger spread of information would lead to more overlapped information and strengthened 'data redundancy' and hence a more rapid reduction in observational influence. Thus, theoretically, the PAI of broader features (winds here) would increase more rapidly with the decrease in observational density compared to the PAI of *h* and *r*.

However, the lines in Figure 5.4 show the opposite situation that the PAI increase more rapidly for *r* and *h* with decreased density of observations than for the winds. The Hovmoller plots of observational influence of *r* (Figure 5.6) show in detail the spread of information with two different observational densities in the presence of rainfall. Indeed, the observational influence increases in convective regions as the observation is less dense, but the changes seem insignificant compared to change in magnitudes for v when reducing the observational density (see the change of magnitudes of colour bars

in Figure 5.5). Moreover, the regions of high values seem broader in the lower panel but this could be explained by the fact that the resolution of the plot has changed as less pixels are in the lower panel. This is consistent with the spatial propagation of information being limited where convection is initialised, so that denser observations still being able to provide independent information which would not cause too much variation in PAI. Therefore, the rapid increase in PAI for rain as the density is reduced seen in fig 5.4 is highly related to the large balanced regions where the spread of information is further, providing more overlapped information at high observational densities. Therefore, high-resolution observations seem more significant in convective regions than steady regions.

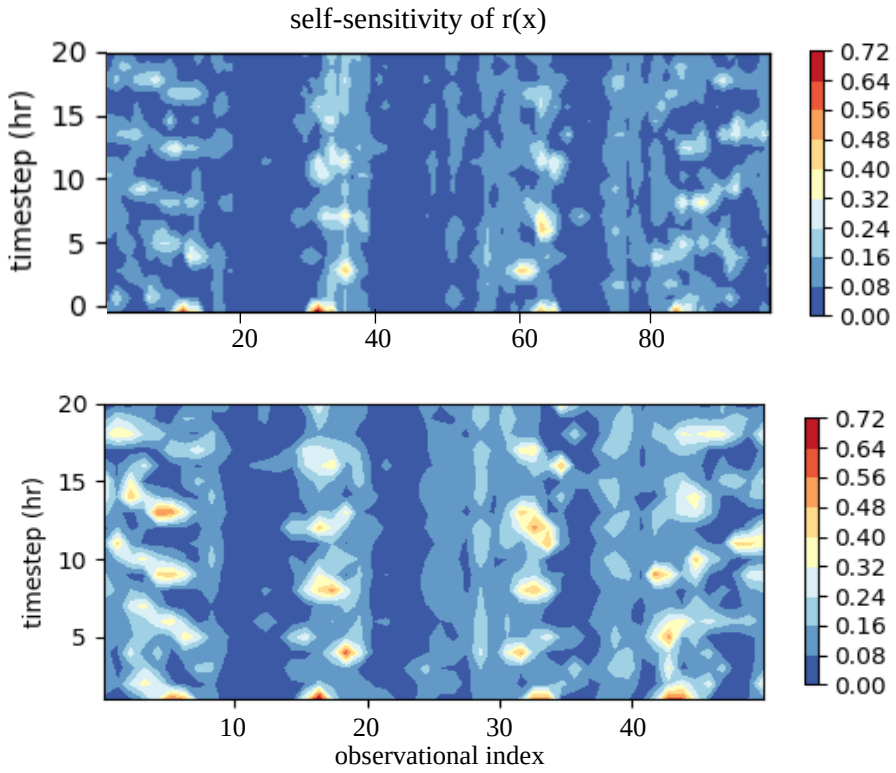

Figure 5.6: Hovmoller plot of self-sensitivity of rainfall at observational density equals to 5 km (top) and 10 km (bottom). The x axis represents the index of observation throughout the domain.

Furthermore, back to the parabolic trajectories in Figure 5.4, the PAI for most variables is more sensitive to the change of observational density in data rich areas but changes mildly when the observational intervals reach a certain value (e.g. 50 km for r). This gives inspiration for finding an optimal density of observations in NWPs, at which

plenty of information can be provided with a minimum cost of producing the observations. The idea of optimal sampling will further be discussed in Section 6.

5.1.3 Cross sensitivity between observations

Investigations of the cross-sensitivity benefits the understanding of the how the information of one observation type propagate to the other variables. The cross-sensitivities of the variables in rotating flow is exhibited in Figure 5.7. We see that the cross-sensitivities between *h* and *r* are highly consistent with the regions of convection (see Figure 5.1), implying that observation of *r* strongly constrains the analysis of *h* and vice versa. The other cross-sensitivities do not appear to show such a strong signal. In the following section we investigate how the observation influence changes if observations of pressure, the most informative observational type from section 5.1.2, are removed out of the system.

In Figure 5.8 the PAI of the observations is recalculated after the extraction of *h* observations. We see that the influence of the remaining variables increases parabolically with the drop of observational density, similar with the situation when all the variables are present. Notably, the removal of the *h* observations does not significantly affect the OID, implying that the loss of the value brought by one observation will be compensated by other types of observations. Moreover, the influence of the observations of winds in this new system, particularly the transverse wind, is more sensitive to the variation of observational density, compared to the previous observational system. This change highlights the interactions between the influence of *h* and *v*, which will be discussed further below.

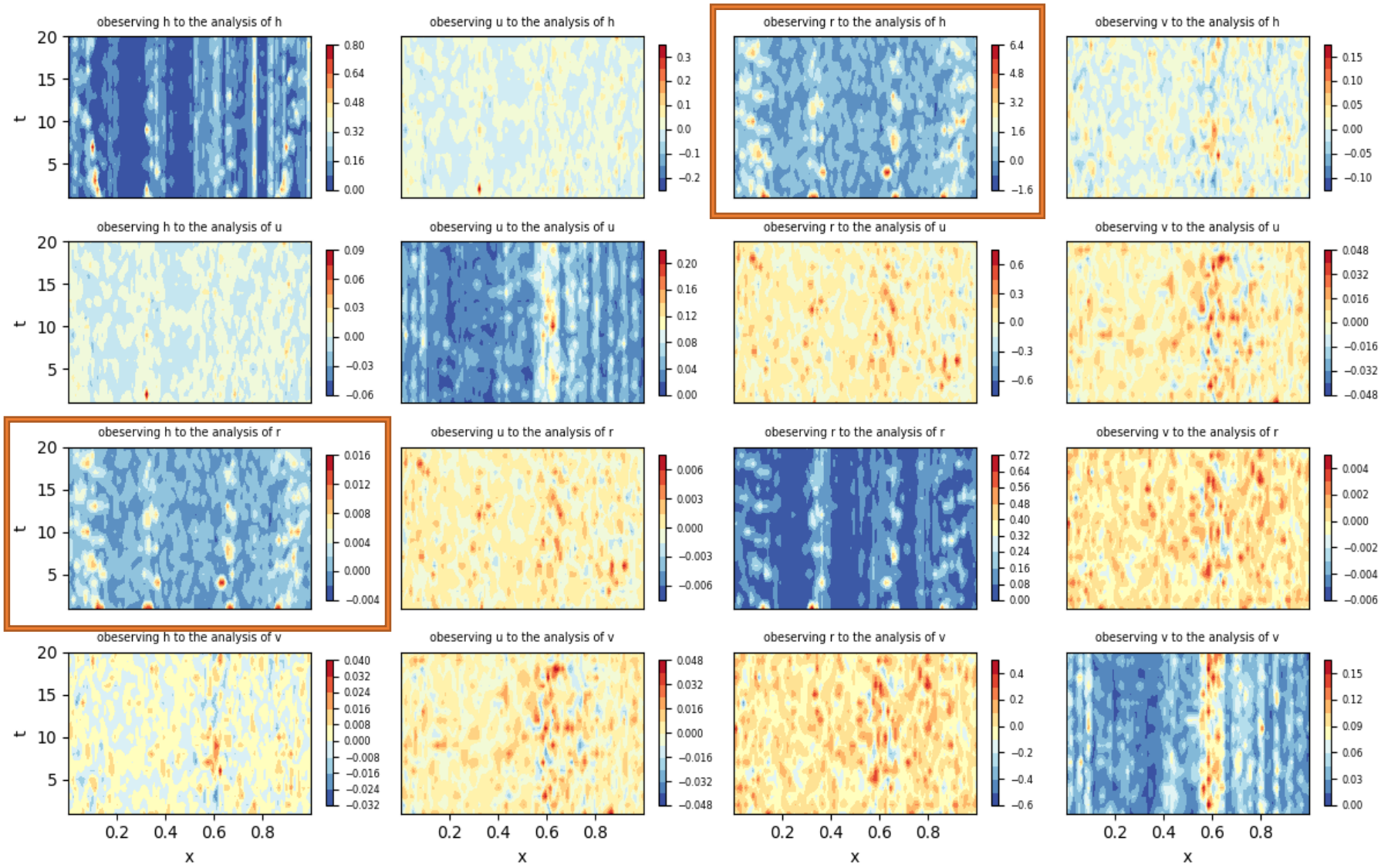

Figure 5.7: Hovmoller plot of influence of the observations to the analysis of each variable, with the observational interval at 5 km.

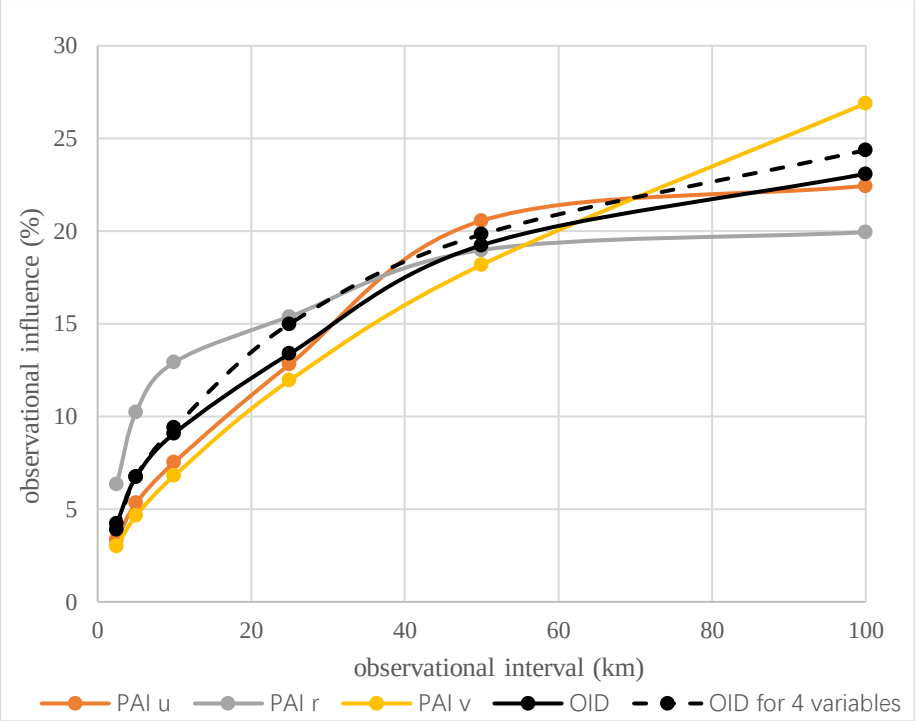

Figure 5.8: The PAI of each variable and OID of the observational system at different observational densities with the removal of observations of *h*, and the OID when *h* is observed (the dotted line).

According to the comparison of the analysis sensitivity of *h* to the observation of *r* with and without the presence of observed *h* (Figure 5.9), the analysis of *h* depends highly on the observation of rainfall close to the convections after removing the observation of *h*, which means the observations of rainfall contributes to the analysis of *h* at convective scales. Whereas in regions away from the convection, the sensitivities remain close to zero, implying that the observation of *r* is not so useful in terms of providing a kind of replacement to *h* observation. Besides, the higher influence in convective regions than in steady regions also confirms the conclusion from section 5.1.2 that the information propagating across variables has a limited spatial spread in unbalanced regions.

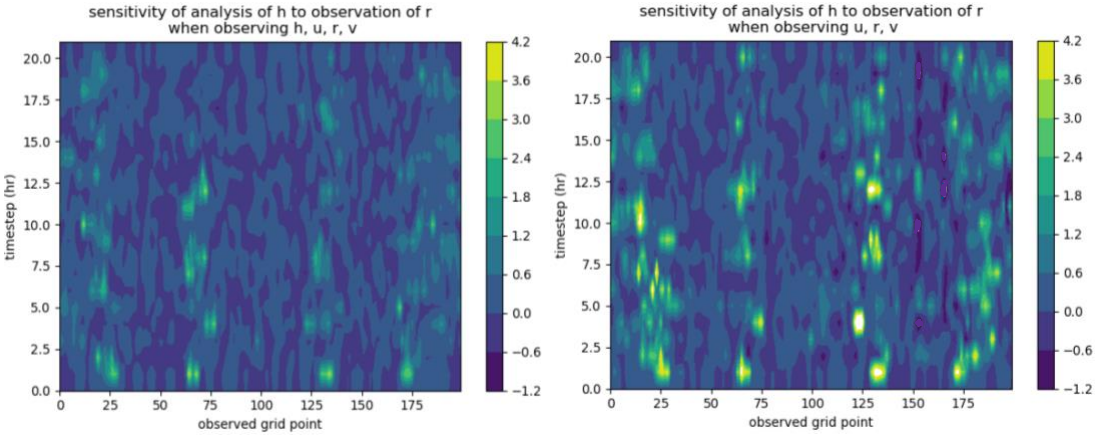

Figure 5.9: Hovmoller plot of sensitivity of analysis of pressure to the observation of rain mass with (left) and without (right) the observation of pressure. The observational interval is 2.5 km.

Another interesting interaction lies between the observational influence of *h* and *v*. As discussed above, the PAI of *v* increases rapidly when the observation of *h* is excluded, indicating the potentially rising influence of *v* observations to the analysis of *h*. This is also demonstrated in the top two graphs in Figure 5.10 which shows the change of the sensitivity of analysis of *h* to the *v* observations after removing the *h* observations. Obviously, the value increases for some regions, which means the same perturbations in the observations of *v* would lead to a larger variation of analysed *h*, so that the analysis of *h* becomes more sensitive to the observations of *v*. Moreover, in rotating flow, *h* and *v* are linked by geostrophic balance (Eq 5.1) in steady regions. Therefore, theoretically in these regions the observation of *v* will be more beneficial to the analysis of *h*, compared to places with large departure from geostrophic balance, and vice versa. However, this is not clear in figure 5.10 particularly for the sensitivity of analysis of *v* to *h* observations (the bottom graphs). This may be because unlike the occurrence of rainfall which is directly controlled by *h* exceeding the thresholds, in geostrophic balance, *v* is directly associated with only the gradient of *h* rather than *h* itself. Also, it is not strictly balanced over the steady regions due to the occurrence of small disturbances which are unobvious compared to the very large departure of geostrophic balance in convective regions.

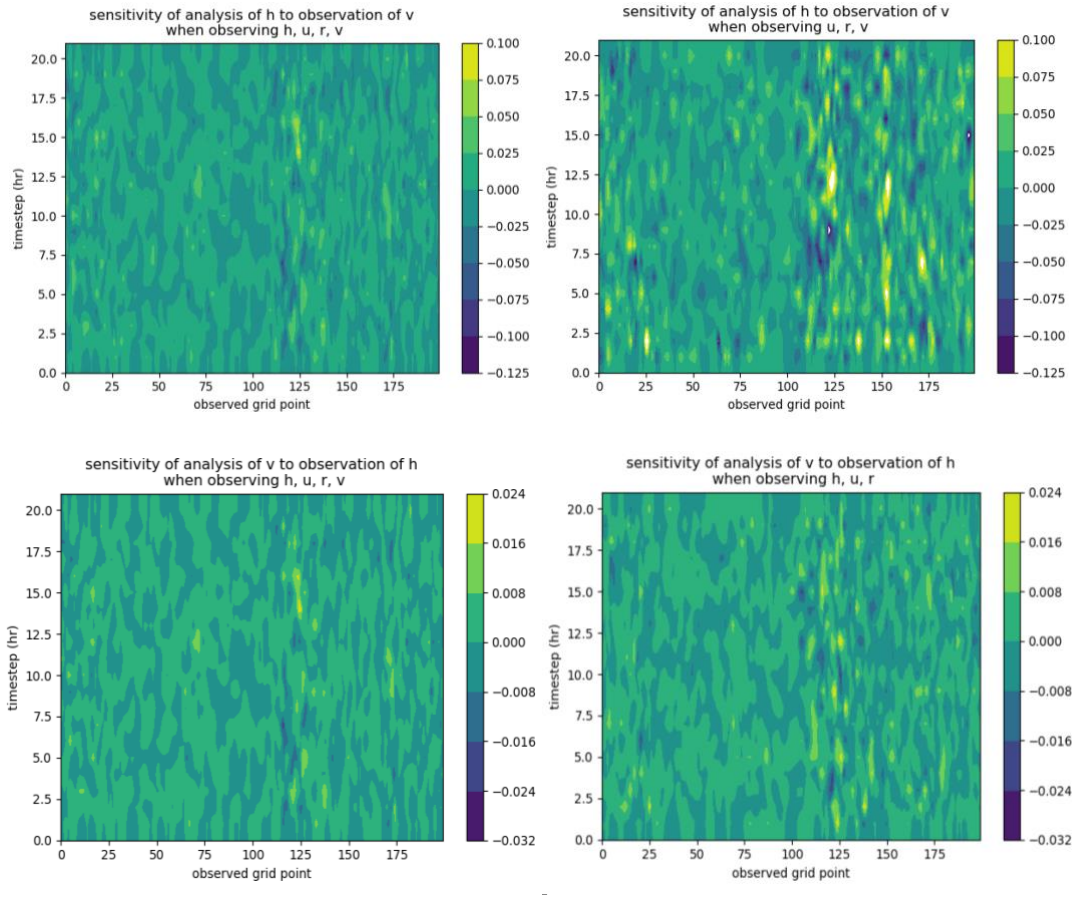

Figure 5.10: Hovmoller plot of sensitivity of analysis of *h* to the observation of *v* with (top left) and without (top right) the observation of *h*, and the sensitivity of analysis of *v* to the observation of *h* with (bottom left) and without (bottom right) the observation of *v*. The observational interval is 2.5 km.

5.1.4 Ensemble performance and the accuracy of the analysis

Within this section we explore the link between observational influence and the accuracy of the analysis. As described in Section 4, SPR and RMSE are applied to test whether observations are assimilated in the right way to improve the accuracy of the analysis. Firstly, we consider the relationship between ensemble spread and the observational influence. According to Eq 3.11, the gain matrix **K** is directly calculated from the forecast error covariance $\boldsymbol{P}_e^f$ which is derived from the model forecast ensemble: the increase in $\boldsymbol{P}_e^f$ will lead to a corresponding increase in **K** and hence the influence matrix **HK**. Then the self-sensitivities should be related to the SPR_*fc* which approximates to $\sqrt{\frac{1}{n}Tr\left(P_e^f\right)}$ (Eq 3.16). This relationship is confirmed in Figure 5.11, in which the SPR_*fc* and self-sensitivities of the four variables in rotating flow are plotted.

High observational influence occurs where the SPR_*fc* is large, implying that the observation becomes more valuable where large disagreement between forecast ensemble members occurs. Moreover, Eq 3.12 links the observational influence to the analysis error covariance $\boldsymbol{P}_e^a$, as well as to the SPR_*an* (Eq 3.17). Eq 3.12 can be transformed into: $\boldsymbol{P}_e^f - \boldsymbol{P}_e^a = \mathbf{KH}\boldsymbol{P}_e^f$, indicating that the largest observation influence is expected to be found where the largest reduction in analysis spread compared to the forecast spread occurs. It is also demonstrated in the middle column of Figure 5.11 that the reduction in SPR_*an* is large compared to SPR_*fc* where SPR_*fc* and self-sensitivities are large. This means when the forecast error covariance is large, the role of observations is more significant in reducing the analysis error covariance.

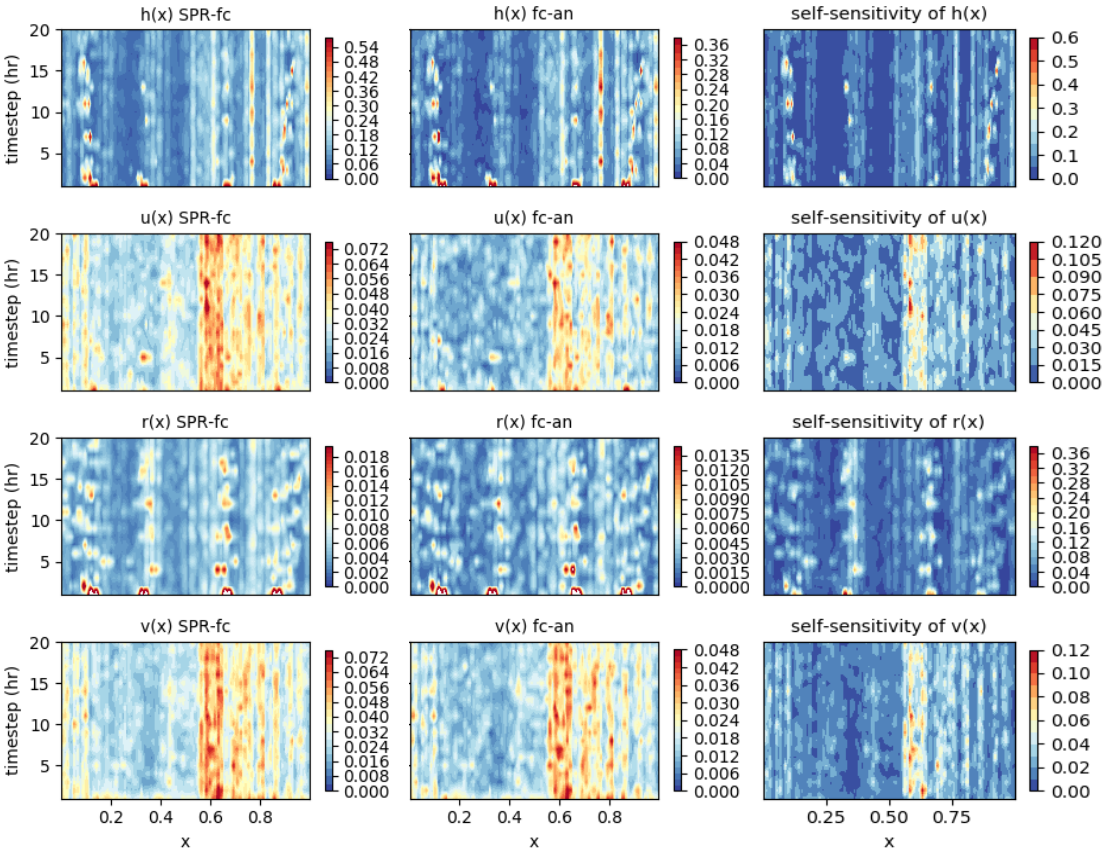

Figure 5.11: Hovmoller plot of SPR of the forecast (left column), the difference between SPR_*fc* and SPR_*an* (middle column), and self-sensitivity (right column) of each variable, with the observational interval at 2.5 km.

Moreover, the pressure and rain mass rows in the same figure exhibit the signals of convections, implying that forecasting the convection and precipitation is a large source

of uncertainty in the system. The observations are important in constraining this and leading to a larger reduction in analysis uncertainty. It is more predictable in terms of the large balanced areas as the ensemble has less uncertainty there and the observations are less weighted in DA. When looking at the wind panels, however, the observations are of significance particularly near x = 0.6, and in the same region the SPR_*fc* also shows large discrepancy which is not related to the occurrence of convections or any ageostrophic features. This suggests the ensemble does not provide a true reflection of the model uncertainty especially in wind fields.

As for the analysis system, RMSE is a diagnostic to evaluate the analysis accuracy compared to the truth, according to which we can estimate where the spread of the analysis ensemble is expected to be sufficient. As mentioned in Section 4, the spread should be comparable to the RMSE for the ensemble to adequately estimate the error. As shown in Figure 5.12, the RMSE for *h* and *r* captures the features of departures from geostrophic balance, showing a larger inaccuracy of model analysis in these regions. If the ensemble spread is accurate then we would expect the SPR and hence observational influence to be high in the same regions where the RMSE is high. Therefore, the magnitude of difference between RMSE and SPR is expected to be zero. However, from the right column of figure 5.12, we see that as for the difference in *h* and *r* panels, it is close to zero in most steady regions, while particularly large in convective regions. Also, the magnitudes of difference in convective regions are comparable to the RMSE, indicating an extremely insufficient spread there. This can also be confirmed by comparing the RMSE with the Hovmoller plots of SPR in the same figure: the SPR at convective cores can be ten times less than RMSE. Therefore, the observation has less influence in convective regions than it would do if the spread correctly represented the RMSE. On the other hand, the SPR is comparable with RMSE over the remaining balanced regions, and both of them are at a small magnitude, indicating that although the observation influence is small, the observations are assimilated in an optimal way. Similarly, for the wind variables the spread in the ensemble underestimates the RMSE. However, the RMSE for winds corresponds less with the features of convections, and the difference between RMSE and SPR is distributed more evenly through the domain.

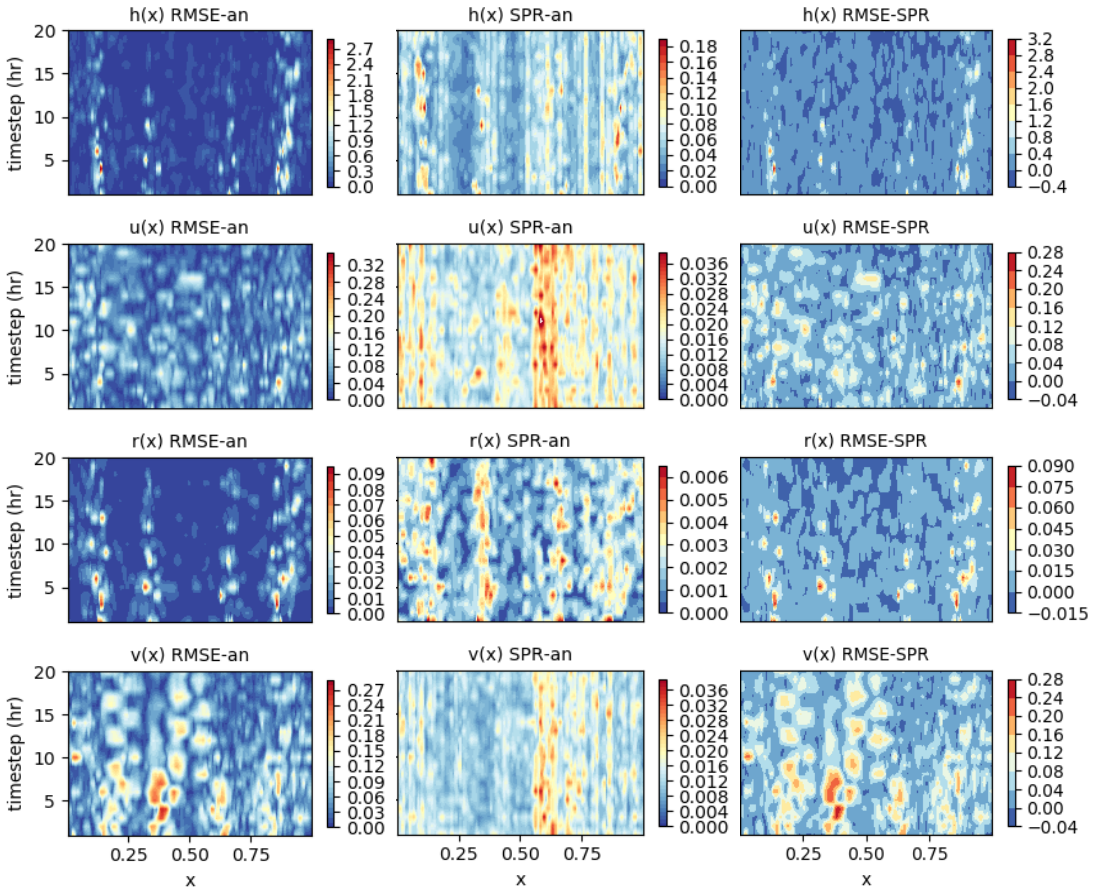

Figure 5.12: The RMSE of analysis (left column), the SPR of analysis (middle column), and the deference between the RMSE and SPR_*an* (right column) for four variables.

The spatially averaged SPR and RMSE of the variables at each DA cycle are plotted in Figure 5.13. The two lines are divergent throughout the assimilation period for each variable, with the SPR remaining at a constant small value, illustrating that the ensemble spread is insufficient compared to its error. As the observational influence depends on the SPR rather than RMSE, it can be concluded that because the SPR systematically underestimates the forecast uncertainty then the observations will have systematically less influence than they should in a well-tuned system. Therefore, the observation influence diagnostic may have limited value when used to make decisions, for example, about the design of future observing networks.

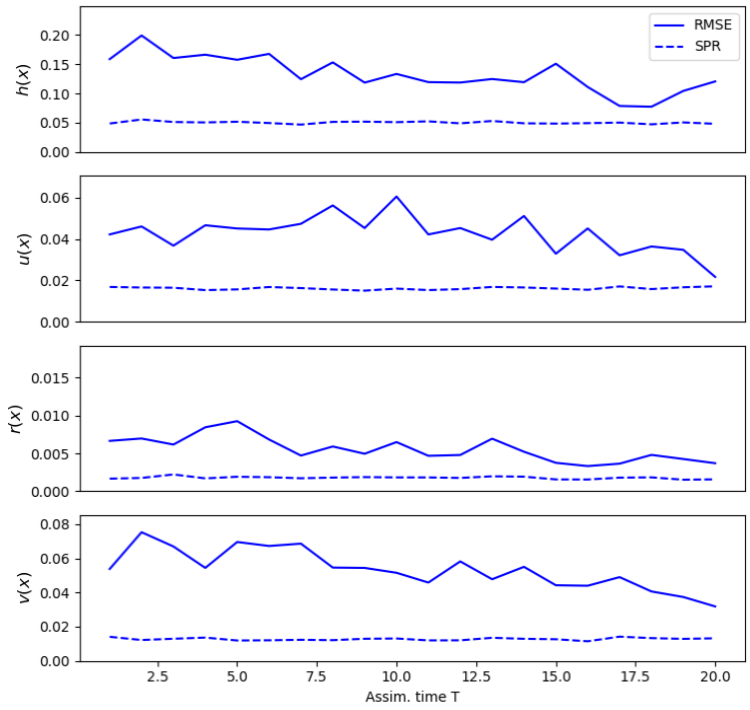

Figure 5.13: The mean RMSE and SPR of analysis of the variables at each timestep.

In operational NWP, the problem of not having enough spread in the ensemble due to the under-sampling is common. Bonavita *et al.*, (2012) found the global-averaged spread of the ECMWF ensemble DA system to be half the value of forecast error, and Houtekamer and Zhang (2016) similarly found that only a quarter of the error variance of ensemble mean is explained by the ensemble spread. To compensate for this, the ensemble perturbations can be inflated to maintain sufficient spread. Within these experiments, the choice of inflation parameters is based on the DA experiment in Kent *et al.*, (2017). This results in the magnitude of SPR being only at around 1/3 of that of RMSE for most variables, indicating that inflation factors are not well tuned for this case. It is hard to find an inflation factor that is optimal in all the cases due to the changes in variables and model dynamics, but fortunately, using the same inflation factors, a better tuned example is provided in the next case of non-rotating flow over topography.

5.2 Non-rotating flow over topography

The observing system for non-rotating case is simpler than rotating scenario, as the transverse velocity is removed from the system. In the same way, we start with the dynamic of the scenario. Figure 5.14 shows the free surface height $h(x)+b(x) > Hr$, and wind convergence $-\partial_x u > 0$, as well as the evolution of rain $r(x)$ through time. The production of precipitation requires both the exceedance of threshold heights and the wind convergence, and the rate of rain is proportional to the strength of wind convergence. Also, there are black dots in wind panel showing extremely large wind convergence that propagates to the right. From the top panel, it can be seen that the free surface height exceeds the precipitation threshold mainly in two regions: one is directly above the ridge (the ridges are located from x~0.2 to x~0.5, see Figure 3.4), and the other is downstream from the ridge where the wave propagates to the right. Rain correspondingly propagates with the convective columns. This matches very well with the lee-side enhancement mentioned in Houze (1993) that the propagation of deep convections and clouds downstream from the ridge is a characteristic orography-induced phenomenon, confirming the well-built model dynamics.

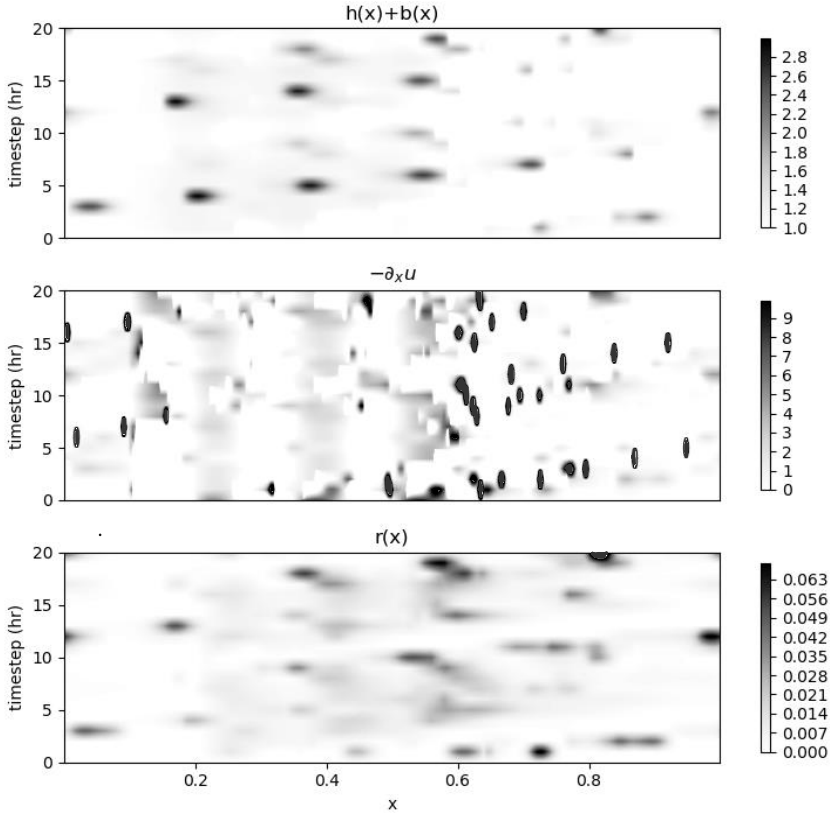

Figure 5.14: Hovmoller plot for non-rotating flow over topography, highlighting the condition for initiation and the sequent evolution of convection. From the top to bottom: $h(x)+b(x)$, $-\partial_x u$, and $r(x)$.

It should be noted here that the production and removal of rain is controlled by the parameters α and β in (Eq 3.2d), and water mass potential coefficient ${c_0}^2$ in (Eq 3.2d). Using different values of these parameters would lead to different solutions not only for rain but also for other variables, due to the coupling in (Eq 3.2b). Therefore, they can be tuned for different DA experiments as desired.

5.2.1 Analysis sensitivity to observations

The observational system for nonrotating flow is slightly simpler than that for rotating scenario, with only three variables being detected: $h(x)+b(x)$, $u(x)$, and $r(x)$. Figure 5.15 shows the evolution of the convection as well as the self-sensitivities of each variable. Unlike the rotating case, the observational influence of h seems random and irrelevant to the exceedance of threshold, with a highlighted band over x ~ 0.8 throughout the period. As discussed in the rotating case, the abnormal concerns put by the ensemble over a fixed location is likely to be caused by the imperfect set-up of the model, which will be further investigated in Section 5.2.3.

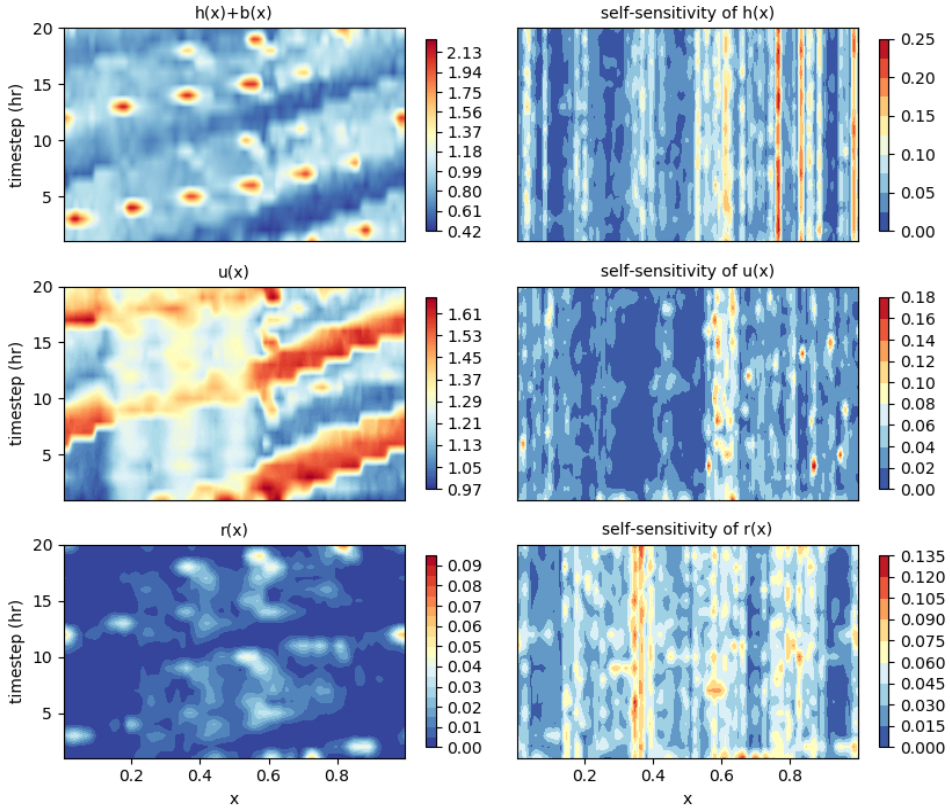

Figure 5.15: Hovmoller plot of the analysis of evolution of convections (left column) and the self-sensitivity of each variable (right column) over 20 DA cycles. The variables are observed every 2.5 km.

As for the wind panels, the evolution plot of $u(x)$ shows bands of strong winds propagating to the right. The serration-like lower sides of the bands denote the sudden large convergence of wind, consistent to the black dots in $-\partial_x u$ panel in Figure 5.14. However, due to the block of the topography, the wind does not vary too much over the region of ridges. The self-sensitivities of u exhibit points of high values in the right half of the graph, corresponding to the strong wind convergence in the left column. The value remains small over the ridges where windspeed has weaker variation, indicating that the observational influence is sensitive to the dramatic changes of wind speed. On the other hand, it is hard to find a correspondence between the onset of precipitation and the self-sensitivities of r. The self-sensitivities capture only a few signals of precipitation (e.g. the precipitation at the first timestep between x=0.6-1), while the values in the remaining areas seems irrelevant with convections. However, since the performance of observations are directly related to the SPR of forecast, it might be helpful to take the behavior of ensemble spread into account. The effect of convections to the ensemble and observational influence will be further discussed in 5.2.3.

The overall influence of each variable is calculated for non-rotating flow as well. Figure 5.16 shows the PAI of each variable and the overall influence of the observation system with different observational densities. Similar to the rotating case, pressure is still the most informative variable in the observational system, followed by the rain mass and the winds. The observational influence increases as the observational density is reduced, which has already been explained as the result of data redundancy. Also, the lines are close to each other for high densities, indicating that the observational influence is less associated to variable types when the observation is dense enough to resolve the main features of the convection. However, unlike the rotating case, the increasing rates of h and r behave more gently. This is because the convections and rainfall in this case are more continuous in terms of both spatial and time, compared to the isolated convections in rotating case. The information provided by the observations is independent and has limited spread within the large convective areas, which limits the increasing rate of PAI.

Furthermore, in practice some high-resolution satellites take measurements every 0.25-0.5 degree, which equals to the observational interval at around 25-50 km in midlatitudes. The overall influence at this interval in the figure varies from around 17%

to 20%, similar to rotating case. However, the non-rotating scenario has also been tested by Kent *et al.*, (2020), with the OID for observational interval at 50 km being approximately 30 %, and he also noted that the OID comparable to operational convective-scale NWP is typically between 20% - 40%. The result here and of rotating case are slightly below the typical interval but are still realistic, because the observational density in data-sparse regions could reach hundreds of kilometers in operational system, and the OID calculated at 100 km (~26 %) is within the typical interval.

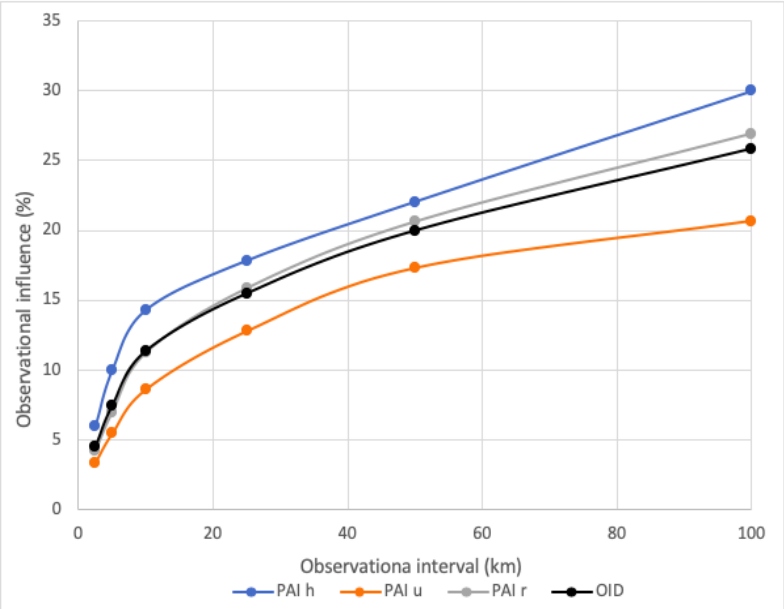

Figure 5.16: The PAI of each variable and OID of the observational system at different observational densities.

5.2.2 Cross sensitivity between observations

In order to estimate the effect of a particular observational type, one way is to remove the relevant observations from the assimilation system and then compare the analysis performance against the control experiment containing all observations. Here the most informative observation type, *h*, is removed to evaluate its impact on the system and to the other variables. Figure 5.17 shows the PAI of *u* and *r* and the OID with and without *h* observations. After removing *h* observations, the influence of wind shows a notable increase, particularly at low observational density, indicating that the observation of *u* contributes a lot to the analysis of *h* which suppresses the observational influence of *u*

itself in the experiment containing *h* observations. Whereas the PAI of *r* firstly increases rapidly without the presence of *h* whilst drop to a lower value than the control experiment as the observations are less dense. The overall influence per observation increase after removing the *h* observations mainly due to the dramatic rise in the influence of *u* when the observational interval is larger than 10 km. However, when the observation interval is less than 10 km, removing observations of *h* has little effect on the OID.

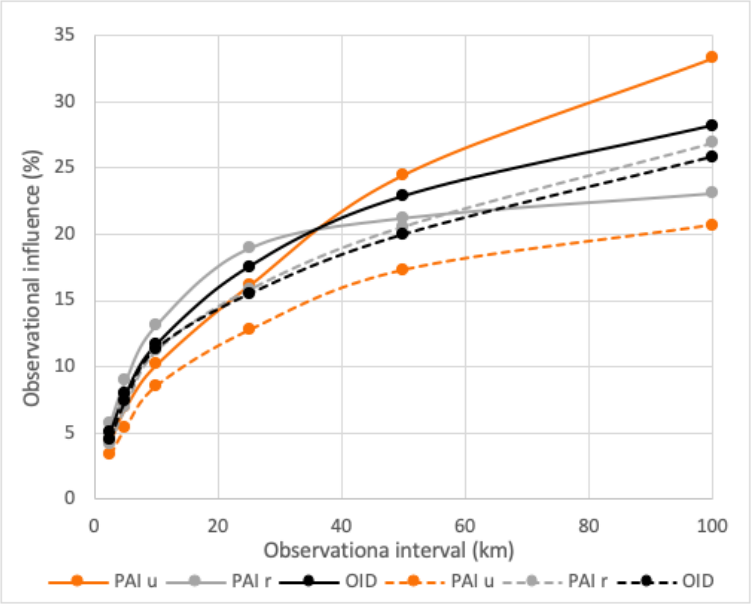

Figure 5.17: The PAI of u and r and the overall influence after removing the observation of *h* (solid lines) and the same diagnostics when all variables are observed (dotted lines).

The impact of observations of *u* and *r* on the analysis of *h* can also be evaluate from the **K** matrix. As shown in the left column (in the presence of the observation of *h*) in Figure 5.18, the diagnostic of sensitivity of analysis of *h* to the observation of *u* is mostly negative, while that of *h* to *r* is positive at most cases. This means the decrease of the observational value of *u* would cause an increase in the analysis of *h*, while the decrease in *r* would lead to the reduction in *h*. Dynamically this make sense: the convergence of the wind would lead to the lift of the free surface height, and the rate of rainfall is proportional to the strength of the convection which is controlled by the degree of the exceedance over the threshold. By comparing the left column with the right column where the observation of *h* is removed, the negative values become more negative and

the positive values are more positive, which means the same perturbation in the observations of the rest variables would lead to a larger variation of *h* so that the analysis of *h* becomes more sensitive to the observations of *u* and *r*.

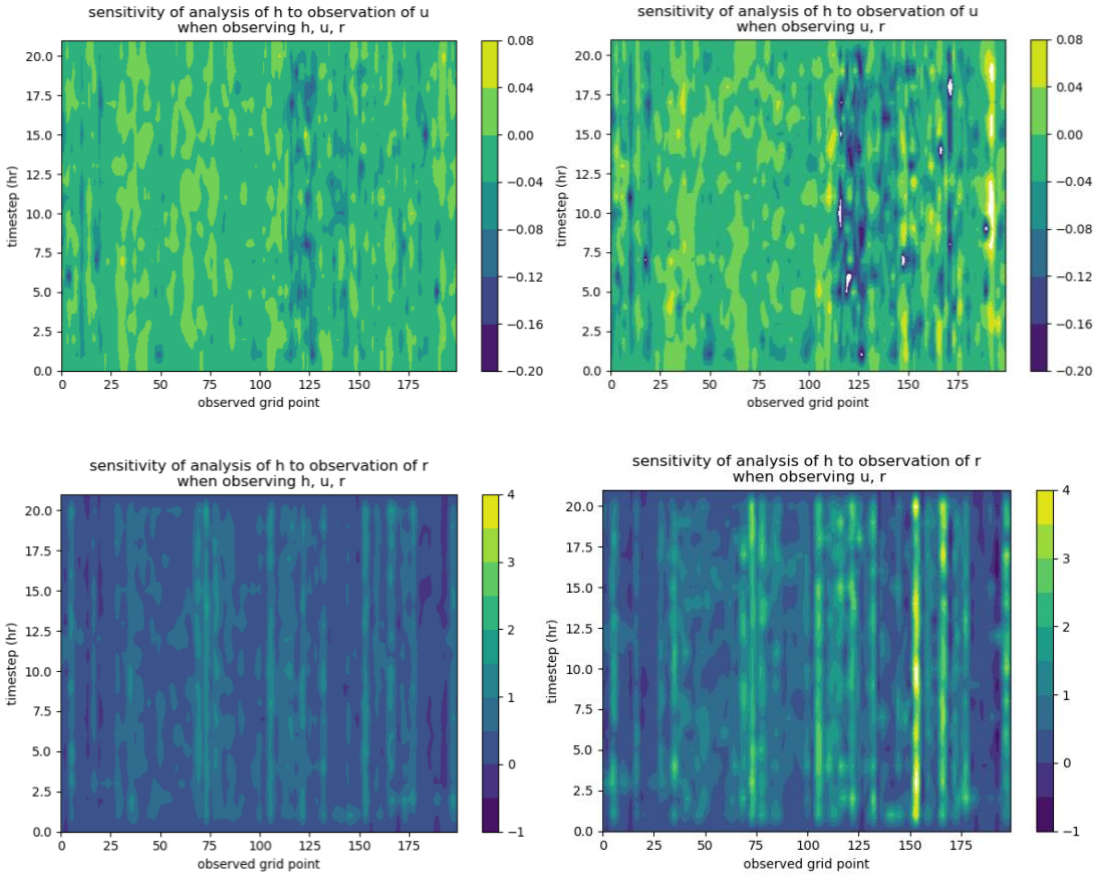

Figure 5.18: Hovmoller plot of sensitivity of analysis of *h* to the observation of *u* with (top left) and without (top right) the observation of *h*, and the sensitivity of analysis of *h* to the observation of *r* with (bottom left) and without (bottom right) the observation of *h*, with the observational interval at 2.5 km.

5.2.3 Ensemble performance and analysis accuracy

As being confirmed in rotating scenario, the observational influence is determined by ensemble spread of the forecast, and this is also verified for nonrotating case in Figure 5.19, where the distribution of SPR_*fc* is highly consistent with that of self-sensitivities of each variable. In addition, the SPR of *u* and *r* panel successfully captures some features of large wind convergence and the rainfall by comparing with the evolution of *u* and *r* in Figure 5.15, illustrating that the EnKF puts uncertainties at rainfall regions and areas with strong wind convergence in this case. However, as for the *h* field, the

SPR does not show obvious features related to the exceedance of threshold, and the ensemble always puts special uncertainties over a few fixed grid points (e.g. the grid points around x=0.8), resulting in the unexpected high observational influence over the same locations. According to the similar features caused by an imperfect ensemble in rotating case, one factor here might be the imperfect additive inflation parameters applied in the experiment.

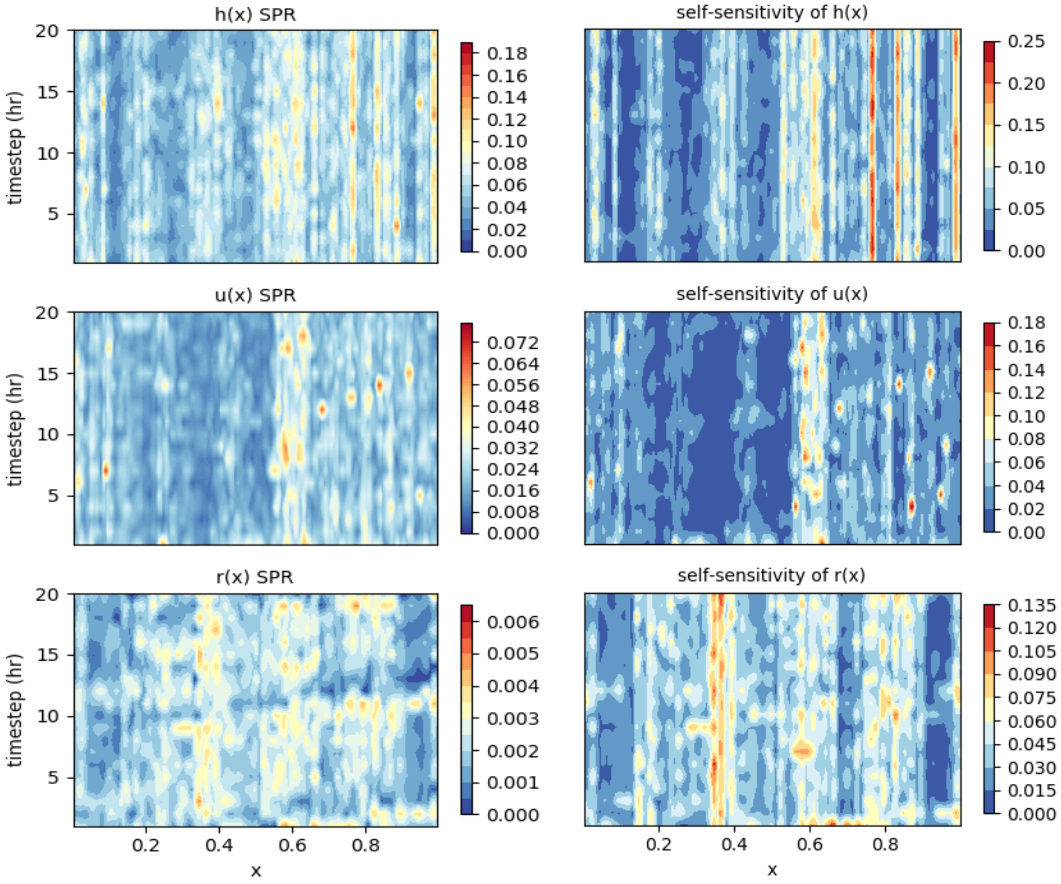

Figure 5.19: Hovmoller plot of SPR of forecast (left column) and self-sensitivity (right column) of each variable for nonrotating flow, with the observational interval at 2.5 km.

In order to test the performance of the EnKF in this case, the evolution of RMSE and the difference between RMSE and SPR at each assimilation cycle is plotted in Figure 5.20. The RMSE captures features of convections and precipitations in the *h* and *r* panels, and features of strong wind convergence from the wind panel. Again, it confirms that predicting the convections or the strong wind perturbations are the major sources of uncertainties of the analysis. Therefore, the spread is supposed to be large in

the same regions for a well-tuned system. By referring to the difference, particularly for the rainfall panel, the difference between the RMSE and SPR shows very weak signals of precipitation, which means that the ensemble puts uncertainties exactly where the analysis has large error. The difference for *u* and *h* is obvious only at regions with very large wind convergence and exceedance of thresholds. The distribution of difference in the remaining regions is quite even with a small magnitude, indicating that the variables in balanced regions are more predictable using only background information. This indicates the spread is adequate enough for the stable and most convective conditions, although still need to improve at regions with very large meteorological variations.

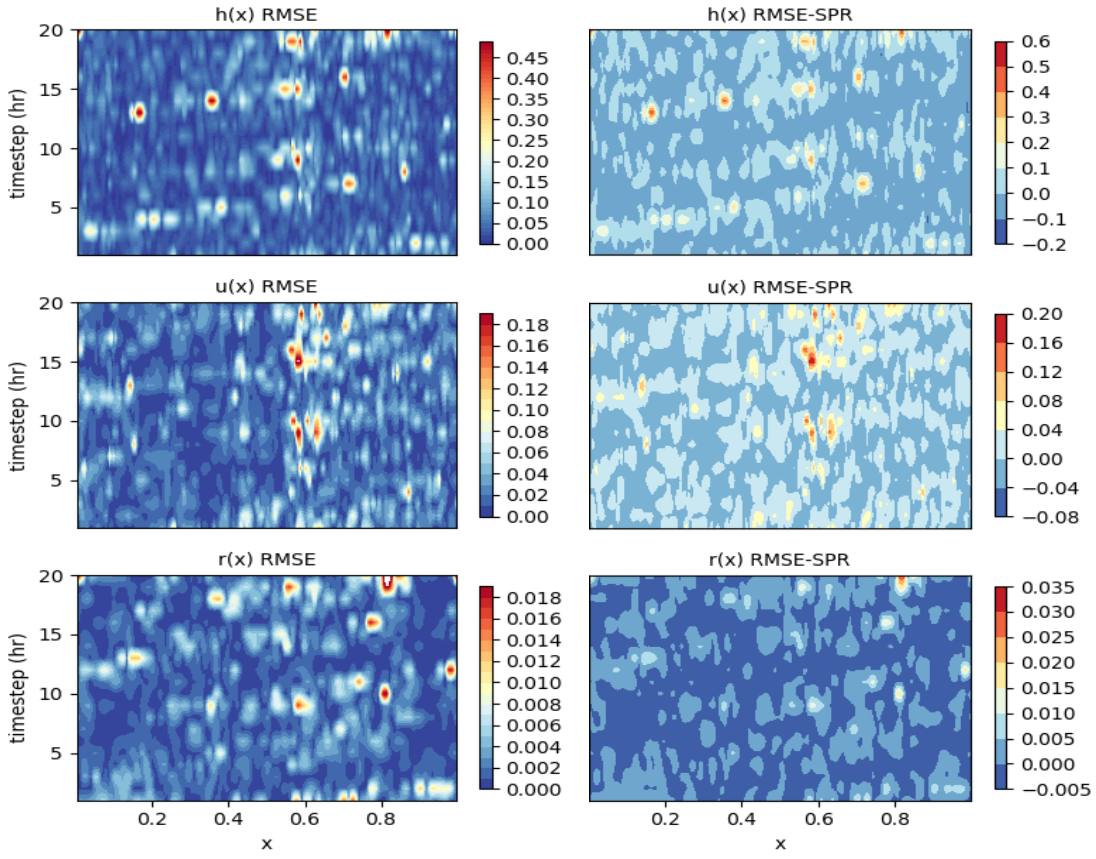

Figure 5.20: The RMSE of the analysis (the left column) and the deference between the RMSE and SPR of analysis (the right column) for three variables, with the observational interval at 2.5 km.

Figure 5.21 illustrates the averaged RMSE and SPR over the domain at each timestep, from which the overall performance of the filter can be seen. The SPR for *u* and *r* seems

comparable with their RMSE, implying that the ensemble is providing an adequate estimation of the forecast error covariance. The SPR for *h* is slightly higher than the RMSE, which means the observations are over-considered by the ensemble. Therefore, observations of *u* and *r* are sufficiently taken into account and better used for forecasting the wind and rainfall than for analysing the pressure. This meanwhile explains the unexpected behaviour of SPR of *h* in the above figures that an imperfect set-up of the model will indeed cause the ensemble putting confidence or uncertainties at a wrong place. It seems hard to find a fixed set-up that can satisfy all the cases. Therefore, the parameters need to be tuned before each experiment.

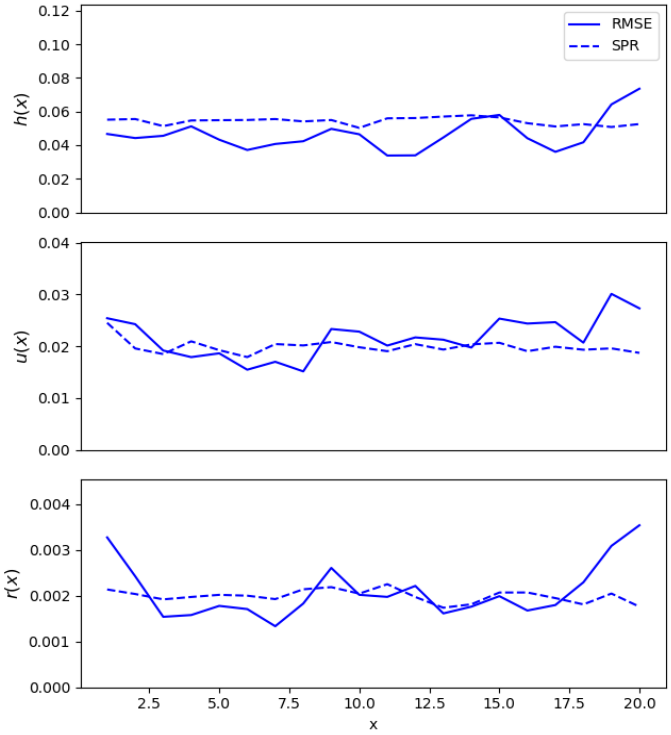

Figure 5.21: The mean RMSE (solid line) and SPR (dotted line) of model analysis for *h* (top), *u* (middle) and *r* (bottom) throughout time.

Generally, there is better agreement between the SPR and RMSE compared to the rotating case, indicating that at this stage of the assessment, a good filter configuration and meaningful observational diagnostic can be achieved within this experimental set-up. Overall, the observing system plays quite an important role in DA in this case, especially in convective regions, indicating the essentiality for putting higher resolution observations according to the OI diagnostic.

Chapter 6

Conclusion and discussion

This study explores the observational influence in a DA system of an idealised fluid model designed by Kent *et al.*, (2017) in the presence of convection and precipitation. The model based on modified SWEs manages to simulate essential aspects of convective-scale dynamics, including the disruption of geostrophic balance and other features related to Rossby adjustment and non-rotating flow over topography. The questions outlined in Chapter 1 are investigated for both scenarios and the results are provided.

How important are the observations of each variable in DA in convective areas?

The observations of pressure and rain mass become increasingly valuable in the DA system closer to the convective cores, and the self-sensitivities of winds are large at places with dramatic variations of windspeed. Whereas the observations are less influential with the value less than 10 % in steady regions. This means that the model analysis in convective regions depends more strongly on the information provided by observations, while the variables in balanced regions are more predictable using only background information.

What are the requirements for the observational density for the different variables?

Following from the previous point, it is necessary to increase number of observations in areas with convection or large variations of wind, such as mountainous or coastal regions. However, it needs to be considered carefully how densely the observational network should be built, since the observational influence is high in data-sparse area and low in data-rich areas due to data redundancy. High density of observations will lead to the large overlap of information and hence limited influence of individual observation, as well as increasing computational cost. Moreover, the optimal density for observations of different variables depends on the scales of the corresponding features. The spread of information is further in board features (e.g. wind fields or steady regions) while being limited in high-resolution features (e.g. convections), affecting the corresponding observational influence.

How much would the influence of the observational system change if one influential observational type is removed?

This study showed that each observational type is capable to influence the analysis of other variables, particularly for pressure and rain mass, and this influence increases in convective regions or when the observations of analysed variables are absent. Additionally, although the pressure is found to be the most informative observational type for both scenarios in this study, the loss of its influence caused by removing it from the observational system can be compensated by the rest of the observational types. The investigation of cross-sensitivities is insightful to the objective use of observations that are of greatest benefits in predicting the corresponding and other variables in operational NWP. This is helpful for handling the vast amount of observational data and easing the computational burden, while retaining the overall influence of observational system.

How does the observation influence correspond to the accuracy of the analysis?

The observational influence diagnostics (non-rotating case in this study) confirm that the observations are important in regions with convection and large variations of windspeed. Also, the observations are found to significantly reduce analysis errors compared to forecast errors in these regions. This gives an alternative way of choosing the particular regions to deploy and assimilate observations by judging the reduction in analysis error. The idea of adaptive observations (Majumdar, 2016) shows the similar concept that observations can be targeted in places where the analysis error are significantly reduced to prevent further rapid growth of forecast errors.

Does each observation give optimal influence on the forecast?

Lastly, this study tested the reliability of observational influence diagnostics by comparing the magnitudes of RMSE and SPR of the analysis. For a well-tuned system, the magnitudes of the two are supposed to be consistent to ensure that the ensemble spread is sufficient exactly where the analysis has errors, and hence the observations are optimally considered in DA. However, in the results of rotating case, the RMSE is divergent with the SPR, showing the insufficient spread of the ensemble caused by a less well-tuned system. Due to this the observations were given progressively less weight in data assimilation, and the observational diagnostics are thus less reliable. The

tuning of the experiment is a major limitation for the rotating case, as it is time intensive to find a set of parameters perfect for both cases.

There are various limitations of this study in answering the above questions that should be noted:

- The model is limited in its representation of the operational DA process because of simplified dynamics and types of observations. The model does not attempt to handle all types of convection that occur in the real world, such as the convection associated with fronts, which is common in UK.
- The observational system is simple, containing only the observations of three or four variables distributed evenly throughout the domain. However, in real situations, observations of rainfall, for example, are typically performed using radar instruments that only return observations when rainfall is present so that the data is not continuous in time and its distribution is not even in space.
- The conclusions so far are based only on a limited number of experiments using specific tuning parameters. The tuning of parameters needs more trials before each experiment to get a good DA performance.

In future work the limitations of the simplified observational system could be addressed by simulating observations that more closely mimic the satellite or radar observational system. This could be achieved by setting nonuniform observations in space and time, and perhaps working with a radiative transfer model to construct a nonlinear observational operator (Kent *et al.,* 2020). This is beyond the scope of this study but is something worth doing to improve the representativeness of the model to the real problems. With more time it would also be beneficial to run experiments under more scenarios to test the robustness of the results and to better tune the DA parameters. For example, these experiments can be extended in operational system to understand how the conclusions apply to operational models and observations. However, it can be foreseen that operational models would increase the difficulty in interpreting the observational influence since they contain more complicated dynamics and observing systems.

Chapter 7

References

Bannister, R. N., Migliorini, S., Dixon and M. A. G., 2011: Ensemble prediction for nowcasting with a convection-permitting model II: Forecast error statistics. Tellus, Series A: Dynamic Meteorology and Oceanography, 63(3), 497–512, doi: 10.1111/j.1600-0870.2010.00500.x.

Baker, N. L., Daley and R., 2007: Observation and background adjoint sensitivity in the adaptive observation-targeting problem. Quarterly Journal of the Royal Meteorological Society, 126(565), 1431–1454, doi:10.1002/qj.49712656511.

Berg P., Wagner, S., Kunstmann, and Shadler, 2013: High resolution regional climate model simulations for Germany: part I—validation. Climate Dynamics, 40, 401–414, doi.org/10.1007/s00382-012-1508-8.

Bouchut, F., Sommer, J., Zeitlin, and V., 2004: Frontal geostrophic adjustment and nonlinear wave phenomena in one-dimensional rotating shallow water. Part 2. High-resolution numerical simulations. Journal of Fluid Mechanics, 514, 35-63, doi:10.1017/S0022112004009991.

Cardinali, C., Pezzulli, S., and Andersson, E., 2004: Influence-matrix diagnostic of a data assimilation system. Quarterly Journal of the Royal Meteorological Society, 130(603):2767–2786.

Clark, Roberts, Lean, P., and Perez, 2016: Convection-permitting models: a step-change in rainfall forecasting. Meteorological Applications, 23, 165–181, doi: 10.1002/met.1538.

de Rooy *et al*., 2013: Entrainment and detrainment in cumulus convection: An overview. Quarterly Journal of the Royal Meteorological Society, 139(670), 1–19.

Evensen and G., 2007: Data assimilation: the ensemble Kalman filter. Springer.

Ford and R., 1994: Gravity wave radiation from vortex trains in rotating shallow water. Journal of Fluid Mechanics, 281, 81-118, doi:10.1017/S0022112094003046.

Fosser, G., Khodayar, S. and Berg, P., 2014: Benefit of convection permitting climate model simulations in the representation of convective precipitation. Climate Dynamics, 44(1–2), 45–60, doi: 10.1007/s0038201422421.

Ha, S. Y. and C. Snyder, 2014: Influence of surface observations in mesoscale data assimilation using an ensemble Kalman filter. Monthly Weather Review, 142, 1489- 1508, doi.org/10.1175/MWR-D-13-00108.1.

Houze and R. A. Jr, 1993: Orographic clouds. In: Cloud Dynamics. Academic Press, San Diego, chap 12.

Houtekamer, P. and Zhang, F., 2016: Review of the ensemble Kalman filter for atmospheric data assimilation. Monthly Weather Review, 144(12), 4489–4532.

Jewtoukoff, V., Plougonven, R. and Hertzog, A., 2013: Gravity waves generated by deep tropical convection: Estimates from balloon observations and mesoscale simulations. Journal of Geophysical Research Atmospheres, 118(17), 9690–9707, doi: 10.1002/jgrd.50781.

Lean, H. W., Clark, P. A., Dixon, M., Roberts, N. M., Fitch, A., Forbes, R., and Halliwell, C., 2008: Characteristics of high-resolution versions of the Met Office Unified Model for forecasting convection over the United Kingdom. Monthly Weather Review, 136(9), 3408–3424.

Lorenz and E. N., 1969: The predictability of a flow which possesses many scales of motion. Tellus, 21, 289–307.

Katzfuss, Jonathan R. Stroud and Christopher K. Wikle, 2016: Understanding the Ensemble Kalman Filter. The American Statistician, 70(4), 350-357, doi:10.1080/00031305.2016.1141709.

Necker, T., Geiss, S., Weissmann, M., Ruiz, J., Miyoshi, T., and Lien, G.-Y., 2019: A convective-scale 1000-member ensemble simulation and potential applications. Quarterly Journal of the Royal Meteorological Society, 146(728), 1423–1442.

Oke, P. R. et al., 2008: The Bluelink ocean data assimilation system (BODAS). Ocean Modelling, 21(1–2), 46–70, doi:10.1016/j.ocemod.2007.11.002.

Pradhan, P. K. et al., 2018: Characteristics of different convective parameterization schemes on the simulation of intensity and track of severe extratropical cyclones over North Atlantic. Atmospheric Research, 199, 128–144, doi:10.1016/j.atmosres.2017.09.007.

Prein, A., A. Gobiet, M. Suklitsch, H. Truhetz, N. Awan, K. Keuler, and G. Georgievski, 2013: Added value of convection permitting seasonal simulations. Climate Dynamics, 41(9–10), 2655–2677.

Prein, A. F. et al., 2015: A review on regional convection-permitting climate modeling: Demonstrations, prospects, and challenges. Reviews of Geophysics, 53, 323–361, doi:10.1002/2014RG000475.

Schroeer, K. and Tye, M. R., 2019: Quantifying damage contributions from convective and stratiform weather types: How well do precipitation and discharge data indicate the risk? Journal of Flood Risk Management, 12(4), 1–13, doi: 10.1111/jfr3.12491.

Stephenson, D. B. and Doblas-Reyes, F. J., 2000: Statistical methods for interpreting monte carlo ensemble forecasts. Tellus A, 52(3), 300–322.

Sun, J. et al., 2014: Use of nwp for nowcasting convective precipitation: Recent progress and challenges. Bulletin of the American Meteorological Society, 95(3), 409–426, doi:10.1175/BAMS-D-11-00263.1.

Tang, Y., Lean, H. W., and Bornemann, J., 2013: The benefits of the Met Office variable resolution NWP model for forecasting convection. Meteorological Applications, 20(4), 417–426.

Kent, Bokhove and Tobias, 2017: Dynamics of an idealized fluid model for investigating convective-scale data assimilation. Tellus A: Dynamic

Meteorology and Oceanography, 69:1, doi: 10.1080/16000870.2017.1369332.

Velleman and Welsh, 1981: Efficient computing of regression diagnostics. The American Statistician, 35, 234–242.

Ward, M., and Dewar, W., 2010: Scattering of gravity waves by potential vorticity in a shallow-water fluid. Journal of Fluid Mechanics, 663, 478-506, doi:10.1017/S0022112010003721.

White. A. A., and R. A. Bromley, 1995: Dynamically consistent, quasi-Hydrostatic equations for global models with a complete representation of the Coriolis force. Quarterly Journal of the Royal Meteorological Society, 121, 399-418.

White. A. A., B. J., Roulstone I. and A., 2005: Consistent approximate models of the global atmosphere: shallow, deep, hydrostatic, quasi hydrostatic and non-hydrostatic. Quarterly Journal of the Royal Meteorological Society, 131, 2081–2107.

Würsch, M. and Craig, G., 2014: A simple dynamical model of cumulus convection for data assimilation research. Meteorologische Zeitschrift, 23(5), 483–490, doi: 10.1127/0941-2948/2014/0492.

Zhang, F., Snyder, C., and Sun, J., 2004: Impacts of initial estimate and observation availability on convective-scale data assimilation with an ensemble Kalman filter. Monthly Weather Review, 132(5), 1238–1253, doi.org/10.1175/1520-0493.